Theory and Applications of Josephson Photomultipliers

by

Luke Colin Gene Govia

A thesis
presented to the University of Waterloo
in fulfillment of the
thesis requirement for the degree of
Master of Science
in
Physics - Quantum Information

Waterloo, Ontario, Canada, 2012

I hereby declare that I am the sole author of this thesis. This is a true copy of the thesis, including any required final revisions, as accepted by my examiners.

I understand that my thesis may be made electronically available to the public.

Luke Colin Gene Govia

Abstract

This thesis describes the back action of microwave-photon detection via a Josephson photomultiplier (JPM), a superconducting qubit coupled strongly to a high-quality microwave cavity, and the applications of these devices. The back action operator depends qualitatively on the duration of the measurement interval, resembling the regular photon annihilation operator at short interaction times and approaching a variant of the photon subtraction operator at long times. The optimal operating conditions of the JPM differ from those considered optimal for processing and storing of quantum information, in that a short T_2 of the JPM suppresses the cavity dephasing incurred during measurement. Understanding this back action opens the possibility to perform multiple JPM measurements on the same state, hence performing efficient state tomography. In addition, this thesis describes the creation of non-classical states of microwave radiation via single photon detection using JPMs. When operated in the low T_2 regime, the back action of a JPM resembles the photon subtraction operator. Using the non-linearity of this back action, it is possible to create non-classical states of microwave radiation, including squeezed vacuum and odd Schrödinger cat states, starting from a coherent state.

Acknowledgements

There are too many people who deserve my thanks for me to ever capture all here, but I'm going to try anyway. So for anyone I miss, I hope you know how grateful I am for your presence in my life.

I'll begin with my supervisor, Professor Frank Wilhelm-Mauch. It has been my pleasure to work for you these past two years; you are truly both a remarkable scientist, and person. You not only possess an encyclopedic knowledge of physics, but are able to inspire and motivate your students to work as hard as you do. You always make your students a priority. My transition to Germany would never have been as smooth were I working for anyone else. I look forward to continuing to work for you for the next three years.

I am greatly in debt to Dr. Emily Pritchett for her continuing support in my academic endeavours. Your dedication and determination, and most of all your passion for physics, is an inspiration for us all.

Though we only worked together for a year, many thanks must go to Dr. Seth Merkel for always making time in his very busy schedule to help the wet behind the ears graduate student that I was.

I am lucky to work with an amazing group of people in the Quantum Device Theory group. Dr. Markku Stenberg, Dr. Mohammad Ansari, Felix, Peter, Farzad, Yuval, Pierre-Luc, Daniel, Wenling, Botan, Fadi and Christine, it has been my pleasure to work with all of you, and I have only benefited from it. On a personal note, special thanks must go to those of you in Germany who have made living in a new place (where I don't even speak the language) so much easier, and so much more enjoyable.

I'd like to acknowledge Deanna Pineau, who began the line of research found in Chapter 2, and whose critiques of the nearly finished product were very beneficial. Your Skype calls, despite the nine hour time difference, were greatly appreciated.

I would like to thank the members of my committee, Professor Norbert Lütkenhaus and Professor Adrian Lupascu, for their guidance over the last two years, and for their patience in dealing with the issues arrising from me spending seven months abroad. I would also like to thank the external reader of my thesis, Professor Marco Piani, for agreeing to do so on such short notice.

The administration staff at both IQC and the UW Physics Department have made things for me much easier than they could have been, and saved me a lot of headache in the process. In particular, I'd like to thank Judy McDonnell, Linda Stadig and Andrew Dale for all their help.

It would be impossible for me to ever capture how grateful I am to have the family that I do. To my parents, thank you for always supporting me, no matter what path in life I choose, and for doing everything in your power to give me every opportunity to succeed. You are always in my corner, and for that I am truly blessed. To my siblings, Leah and Zach, thank you for *never* giving up on me, even when I give up on myself. You two are my rocks.

To all my friends in Trinidad, Canada, and Germany, thank you all for keeping me sane. In particular, to Etienne, thank you for always being only a bbm away, and to the members and coaches of the UW Track & Field Team, I am honoured to have been a member of such a dedicated institution, from which I have gained so much.

Finally, thank you to the stroke of chance that led to me choosing Waterloo's name out of a hat six years ago. It has turned out to be the best decision I never made.

To Colin and Joan.

Table of Contents

List of Figures

Chapter 1

Introduction

1.1 Quantum Information Theory and Computing

The application of quantum mechanics to information theory and practice, such as to the tasks of computation and communication, is the field of quantum information. In many cases, the quantum information theoretic solution to an information theory problem has been shown to be more advantageous than the solution from classical information theory. For example, there exist problems which quantum computers are capable of solving faster than their classical counterparts, with this speed-up being exponential in some cases. In addition, quantum computers are also capable of efficiently simulating quantum systems, something that classical computers are incapable of doing. For more information on quantum computing algorithms, and other aspects of quantum information, see reference [1].

The general circuit model for quantum computing consists of qubits (the quantum analog of classical bits) acted upon by the quantum gates in the circuit. Qubits are controllable two level (or approximately two level) quantum systems, and as their evolution is described by the Schrödinger equation, the quantum gates must be unitary, and therefore reversible. This can

be expressed mathematically as

$$|\psi_{\text{final}}\rangle = \hat{U}_N \hat{U}_{N-1} ... \hat{U}_2 \hat{U}_1 |\psi_{\text{initial}}\rangle \tag{1.1}$$

where $\hat{U}_i$ is the unitary matrix representing the i'th quantum gate. After the desired operations have been performed, the qubits are measured, and the result of the computation obtained.

In many cases however, unitary evolution is insufficient to fully describe a quantum process. This occurs when there are incoherent processes present, such as measurement of auxiliary systems, or decay processes into the environment. To account for this, a more general formulation is needed. In general, we can describe the quantum process by a linear map (often referred to as a superoperator) that takes density matrices to density matrices

$$\rho_{\text{final}} = \mathrm{E}(\rho_{\text{initial}}) \tag{1.2}$$

This map must satisfy two general properties to be a quantum process:

$$1.\ \mathrm{Tr}[\mathrm{E}(\rho_{\text{initial}})] \leq 1 \tag{1.3}$$

$$2.\ \langle\psi| \mathrm{E} \otimes \mathcal{I}_n(\rho'_{\text{initial}}) |\psi\rangle \geq 0 \ \forall\, |\psi\rangle \in \mathcal{H} \otimes \mathbb{C}^n \ \forall n \in \mathbb{Z}^+ \tag{1.4}$$

where $\rho'_{\text{initial}} \in \mathcal{H} \otimes \mathbb{C}^n$ and $\mathcal{I}_n$ is the identity operation on $\mathbb{C}^n$.

The first property ensures that the probability of the quantum process occurring is at most unity (it will generally be less then unity when the process involves measurements), and the second property expresses the fact that the final density matrix is not only positive but completely positive. These properties ensure that E(.) maps the set of density matrices into itself. A map that satisfies these conditions is referred to as completely positive (CP), and a map that also saturates equation (1.3) is referred to as completely positive and trace preserving (CPTP).

Quantum processes are often represented by what are known as Kraus

operators, which are a set of operators $\{\hat{A}_i\}_{i=1}^{D}$ that satisfy

$$\mathrm{E}(\rho) = \sum_{i}^{D} \hat{A}_i \rho \hat{A}_i^{\dagger} \tag{1.5}$$

where $D \leq \dim(\mathcal{H})^2$ for $\rho \in \mathcal{L}(\mathcal{H})$. For a given quantum process, the set of Kraus operators is not unique, and there may exist several distinct sets of operators that satisfy equation (1.5).

Experimentally determining the nature of a quantum process is a task known as quantum process tomography, the goal of which is to obtain a supermatrix that completely describes the action of the map E(.) on density matrices. There are many possible supermatrices that can be chosen, and in this thesis the χ-matrix, a common choice, will be used. The χ-matrix is defined by

$$\mathrm{E}(\rho) = \sum_{ij} \chi_{ij} B_i \rho B_j^{\dagger} \tag{1.6}$$

where $\{\hat{B}_i\}_{i=1}^{\dim(\mathcal{H})^2}$ is a basis for $\mathcal{L}(\mathcal{H})$. The Kraus operators can very easily be obtained from the χ-matrix, as is discussed in section A.2.

Further information on quantum processes can be found in reference [1], and the methodology used to describe the dynamics of general quantum process (i.e. the nature of the map E(.)) will be discussed in section 1.3.

1.2 Circuit Quantum Electrodynamics

Circuit quantum electrodynamics (circuit QED) is the study of the interaction between electrical circuits and electromagnetic radiation in the quantum regime. It is analogous to cavity quantum electrodynamics, with microwave frequency resonators taking the place of optical cavities, and superconducting electrical circuits forming the artificial "atoms". The study

of circuit QED led to the development of superconducting qubits, one proposed architecture for applications in quantum information processing, such as quantum computing.

For the purposes of this thesis, we will consider a single mode microwave resonator operating in the quantum regime. To develop a quantum theory of such a resonator we will follow the methodology of [2] (another good reference is [3]). We begin by decomposing the electric and magnetic fields into their spatial and temporal components (in the absence of any charges or currents, and ignoring polarization) as

$$\vec{E} = \vec{\xi}(\vec{r})e(t) \tag{1.7}$$

$$\vec{B} = \frac{1}{k}\left(\nabla \times \vec{\xi}(\vec{r})\right) b(t) \tag{1.8}$$

where k is the wave number. In this description, Maxwell's equations reduce to two equations for the temporal components

$$\dot{e}(t) = ckb(t) \tag{1.9}$$

$$\dot{b}(t) = -cke(t) \tag{1.10}$$

where c is the speed of light in the resonator material. By the change of coordinates

$$q(t) = \frac{1}{\sqrt{4\pi}ck} b(t) \tag{1.11}$$

$$p(t) = \frac{1}{\sqrt{4\pi}} e(t) \tag{1.12}$$

we can transform equations (1.9) and (1.10) into a pair of equations consistent with the Hamiltonian

$$H = \frac{1}{2}p(t)^2 + \frac{c^2k^2}{2}q(t)^2. \tag{1.13}$$

The Hamiltonian in equation (1.13) is that of a harmonic oscillator with "position" $p(t)$, and "momentum" $q(t)$. Quantizing this Hamiltonian as is

normally done for a harmonic oscillator, we obtain the quantized Hamiltonian of a microwave resonator expressed in terms of the creation and annihilation operators

$$\hat{H} = \hbar\omega \left(\hat{a}^\dagger \hat{a} + \frac{1}{2} \right), \tag{1.14}$$

where $\omega = ck$. The ladder states of the microwave resonator are referred to as Fock states.

As explained in section 1.1, a qubit must be a two level system or an approximately two level system, i.e. one where two levels can be addressed independently of the others. This is obviously not the case for the harmonic level structure of a microwave resonator. In cavity QED atoms are used as qubits, as the anharmonic energy spectrum of atomic energy levels makes addressing only two levels straightforward. This is not so simple to achieve in circuit QED, since the linear nature of most circuit elements leads to harmonic energy level spacing. A non-linear circuit element is therefore needed, and for this purpose, the Josephson Junction is used.

A Josephson Junction consists of two layers of superconducting material separated by a layer of non-superconducting material. One would expect no current flow through such a junction, however, due to quantum tunnelling, Cooper pairs can cross the insulting barrier, and this leads to a non-zero current across the junction. This current is given by the first Josephson equation

$$I = I_c \sin\phi \tag{1.15}$$

where ϕ is the phase difference between the superconducting layers, and I_c is the critical current. If a current above I_c is applied to the Josephson junction, superconductivity breaks down, and equation (1.15) is no longer valid. The voltage across the junction is described by the second Josephson equation

$$V = \frac{\Phi_0}{2\pi}\dot{\phi} \tag{1.16}$$

where $\Phi_0 = \frac{h}{2e}$ is the magnetic flux quantum for superconductors. In light of these equations, the Josephson junction can be modelled as a non-linear inductor in parallel with a capacitor, C_J.

Using Josephson junctions it is possible to build superconducting electrical circuits that have anharmonic energy spectra, and in so doing create superconducting qubits. There are three main classes of superconducting qubits, and this thesis will focus exclusively on one of them, the phase qubit. The phase qubit is a current biased Josephson junction, the circuit diagram for which is shown in figure 1.1.

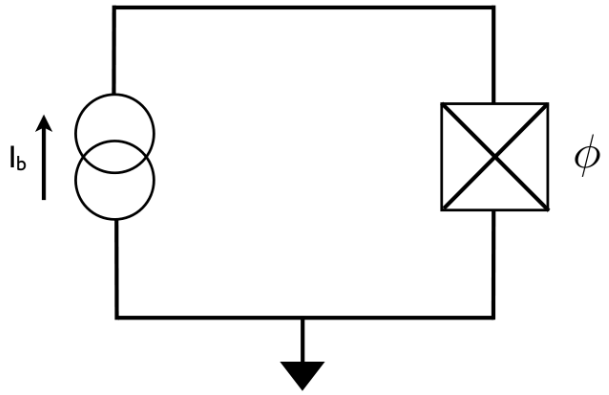

Figure 1.1: The circuit diagram for a phase qubit, where I_b is the applied bias current, and ϕ is the superconducting phase difference across the Josephson Junction.

Using Kirchhoff's laws and equations (1.15) and (1.16) we can derive the following classical equation of motion for the phase qubit

$$I_b = I_c \sin\phi + C_J \frac{\Phi_0}{2\pi} \ddot{\phi}, \tag{1.17}$$

which then leads to the Lagrangian

$$\mathcal{L}\left(\dot{\phi}, \phi\right) = \frac{C_J}{2}\left(\frac{\Phi_0}{2\pi}\right)^2 \dot{\phi}^2 + E_J \cos\phi + I_b \frac{\Phi_0}{2\pi}\phi, \tag{1.18}$$

where $E_J = \frac{\Phi_0}{2\pi} I_c$ is the Josephson energy.

To determine the Hamiltonian for the phase qubit, we define the conjugate momentum of ϕ, $P_\phi = C_J \left(\frac{\Phi_0}{2\pi}\right)^2 \dot{\phi}$. The conjugate momentum is in fact proportional to the Cooper pair difference across the Josephson Junction, $\hbar n = P_\phi$. If we impose the quantization condition $\left[\hat{\phi}, \hat{n}\right] = i\hbar$, where phase and number are now quantum operators instead of classical variables, we obtain the following quantum mechanical Hamiltonian for the phase qubit

$$\hat{H} = E_c \hat{n}^2 - V(\hat{\phi}), \tag{1.19}$$

where $E_c = \frac{(2e)^2}{2C_J}$ is the charging energy, and

$$V(\hat{\phi}) = -E_J \cos\hat{\phi} - I_b \frac{\Phi_0}{2\pi}\phi. \tag{1.20}$$

The phase qubit potential of equation (1.20) is referred to as a tilted cosine washboard potential, and has the shape shown in figure 1.2. This

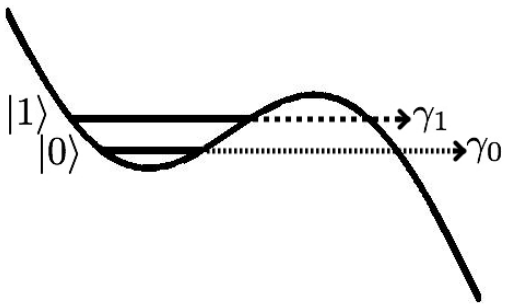

Figure 1.2: The tilted cosine washboard potential of a phase qubit, showing the ground and first excited state, and the finite incoherent tunnel rates out of these states.

potential contains a series of anharmonic potential wells, in each of which

there are quasi-bound quantum states. We choose the ground an first excited state of one such potential well as the logical states of the phase qubit. Since the potential is anharmonic, the transition between these states can be addressed without affecting higher excitation levels.

As can be seen in figure 1.2, due to quantum tunnelling, these quasi-bound states have finite rates at which they can escape the potential well. This rate increases exponentially with excitation number in the well, and can be controlled by changing the barrier height, via manipulating the bias current I_b. This incoherent tunnelling will form the cornerstone of the rest of this thesis.

Now all that remains to be described to characterize our system is the interaction between the microwave resonator and the phase qubit. Restricting to the single potential well of the phase qubit that contains the logical states, we can describe the self evolution of the phase qubit by the Hamiltonian $\hat{H}_{\mathrm{Q}} = \hbar\omega_Q\hat{\sigma}_z$. In as similar manner as a real atom in a cavity, the "artificial" atom formed by our restriction of the phase qubit states will interact with the resonator via a dipole Hamiltonian of the form

$$\hat{H}_{\mathrm{int}} = g\hat{\sigma}_x\left(\hat{a}+\hat{a}^\dagger\right) = g\left(\hat{\sigma}_+ + \hat{\sigma}_-\right)\left(\hat{a}+\hat{a}^\dagger\right), \tag{1.21}$$

were g is the coupling strength, and we have introduced the raising/lowering operators for the qubit, $\sigma_\pm$.

If we assume that the resonator and phase qubit are near resonance, then we can perform the rotating wave approximation (provided $|g| \ll |\omega_{\mathrm{Q}}|, |\omega_{\mathrm{R}}|$) and remove fast oscillating terms in the interaction picture. The interaction between the phase qubit and the microwave resonator is now described by the Jaynes-Cummings Hamiltonian

$$\hat{H}_{\mathrm{int}} = g\left(\hat{\sigma}_+\hat{a} + \hat{\sigma}_-\hat{a}^\dagger\right) \tag{1.22}$$

which preserves the number of excitations in the total system.

1.3 Open Quantum Systems

In this section we generalize the concept of a quantum process to include time dependence, in order to solve for the dynamics of a system interacting incoherently with its environment. This section follows both [4] and [5], which are excellent sources for further information.

We begin by defining a quantum dynamical semigroup, which is a continuous set of linear maps $\{\mathrm{E}_t\}$, parameterized by the time, t, that satisfy the following conditions:

1. $\forall\ t$, E_t is a CPTP map.
2. $\mathrm{Tr}[\mathrm{E}_t(\rho)\hat{O}]$ is continuous in t for all valid ρ and any $\hat{O} \in \mathcal{L}(\mathcal{H})$.
3. E_t is Markovian, i.e. $\mathrm{E}_{t+\tau} = \mathrm{E}_t \circ \mathrm{E}_\tau$ and $\mathrm{E}_0 = \mathcal{I}$.

Here $\mathcal{I}(\rho) = \rho$ is the identity map. We can express any member of a quantum dynamical semigroup as $\mathrm{E}_t = e^{\hat{S}t}$ where $\hat{S}$ is the generator of the semigroup. Combining this with equation (1.2) allows us to define a dynamical equation for the system state $\rho_S(t)$

$$\dot{\rho}_S(t) = \hat{S}\rho_S(t). \tag{1.23}$$

This is known as a Markovian quantum master equation.

The generator $\hat{S}$ is itself a linear superoperator, and the most general form of the right hand side of equation (1.23) is

$$\hat{S}[\rho_S(t)] = -i[\hat{H}_S, \rho_S(t)] + \sum_\mu \gamma_\mu \left(\hat{J}_\mu \rho_S(t) \hat{J}_\mu^\dagger - \frac{1}{2}\{\hat{J}_\mu^\dagger \hat{J}_\mu, \rho_S(t)\} \right). \tag{1.24}$$

The first term in equation (1.24) is just the Liouville-von Neumann equation for coherent evolution under the action of the system Hamiltonian $\hat{H}_S$. Each

component in the sum of the second term is referred to as a dissipator, and each contains a Lindblad operator $\hat{J}_\mu$.

Each Lindblad operator, and its corresponding dissipator, describe a different incoherent process (eg. energy relaxation, dephasing), usually involving interaction with the environment. The form of the Lindblad operator depends on the details of the incoherent process, and γ_μ describes the rate of this incoherent process. A master equation written in the form of equation (1.24) is said to be in Lindblad form.

It is possible to derive a Lindblad form master equation starting from a microscopic description of the system and its environment, $\rho(t)$, and their interaction Hamiltonian $\hat{H}_I(t)$. This process, described in [4], takes as its starting point the Liouville-von Neumann equation for the total system

$$\dot{\rho}(t) = -i\left[\hat{H}_I(t), \rho(t)\right], \tag{1.25}$$

and then proceeds to trace out the environment, under a number of approximations, and finally arrive at an equation of the form of equation (1.24). The three key approximations are:

1. The Born Approximation: $\rho(t) \approx \rho_S(t) \otimes \rho_E$. The environment is only negligibly affected by its interaction with the system.

2. The Markov Approximation: The state of the system at time τ does not affect the dynamics of the system at time t. This implies that any memory effects in the environment dissipate on a timescale too short to observe.

3. The Rotating Wave Approximation

There are several ways to justify these approximations, and for the purpose of this thesis, we will assume the weak coupling limit. This implies that the coupling constant between the system and the environment is very small, and in this regime the Born-Markov approximation, and the RWA are valid.

1.4 Quantum States of Electromagnetic Radiation

The first set of quantum states of EM radiation of interest are the Fock states, which, as previously described, are the ladder states of the Hamiltonian $\hat{H} = \hbar\omega\hat{a}^\dagger\hat{a}$. They satisfy the relations

$$\sqrt{n+1}\,|n+1\rangle = \hat{a}^\dagger\,|n\rangle \tag{1.26}$$

$$\sqrt{n}\,|n-1\rangle = \hat{a}\,|n\rangle \tag{1.27}$$

and are non-classical states of EM radiation, in that they cannot be generated by classical currents. The Fock state $|n\rangle$ corresponds to the quantum state of n photons in the resonator, and the state $|0\rangle$ is the vacuum state.

The quantum states closest to classical states of EM radiation are known as the coherent states. They are defined by

$$|\alpha\rangle = e^{-\frac{|\alpha|^2}{2}} \sum_{n=0}^{\infty} \frac{\alpha^n}{\sqrt{n!}}\,|n\rangle\,, \tag{1.28}$$

where $\alpha \in \mathbb{C}$ and $|\alpha|^2$ is the average photon number of the coherent state. They are the right eigenstates of the lowering operator, with eigenvalues α, and can be thought of as the result of a classical driving field applied to the vacuum. This classical driving field is described by the displacement operator, $D(\alpha) = e^{\alpha\hat{a}^\dagger - \alpha^*\hat{a}}$, which satisfies the relations

$$D(\alpha)\,|0\rangle = |\alpha\rangle \tag{1.29}$$

$$D(\alpha)\,|\beta\rangle = |\alpha+\beta\rangle \tag{1.30}$$

Non-classical states of EM radiation are interesting for several reasons. From a purely foundational perspective, the creation of non-classical states is a direct test of the validity of quantum mechanics, and the creation of non-classical states on a macroscopic scale allows one to probe the quantum-classical transition. Non-classical EM states are also useful and often required for many applications in quantum communication and computation, in particular when entanglement is required.

Two non-classical EM states of particular interest are the even (+) and odd (−) Schrödinger cat states, which are superpositions of coherent states with opposite phase

$$|\Psi_{\pm}\rangle = \frac{1}{\sqrt{N}} \left(|\alpha\rangle \pm |-\alpha\rangle \right). \tag{1.31}$$

These states are interesting as they are superpositions of classical states, and so for large α they represent macroscopic quantum superpositions, and thus, push the boundary of the quantum-classical transition.

A useful way to visualize quantum EM states is through the use of a quasi-probability distribution, which is a graphical representation of a quantum state as a two dimensional surface. There are several kinds of quasi-probability distributions, and the one chosen in this thesis is the Husimi Q function [6], defined by

$$Q(\alpha) = \frac{1}{\pi} \langle \alpha | \rho | \alpha \rangle . \tag{1.32}$$

As the coherent states form an over complete basis for Hilbert space, the Q function will completely characterize any state (the over complete nature of the coherent state basis is also the reason the Q function is not a true probability distribution).

Unlike some other quasi-probability distributions, the Q function exists for all valid quantum states, and is strictly non-negative and bounded. The Q function was chosen as it is a convenient way to describe quantum states that are superpositions of coherent states, as each coherent state component will form a peak in the distribution. As an example, the Q function of an odd Schrödinger cat state (with $|\alpha| = 1$) is shown in figure 1.3, and the two peak structure of the distribution is clearly visible.

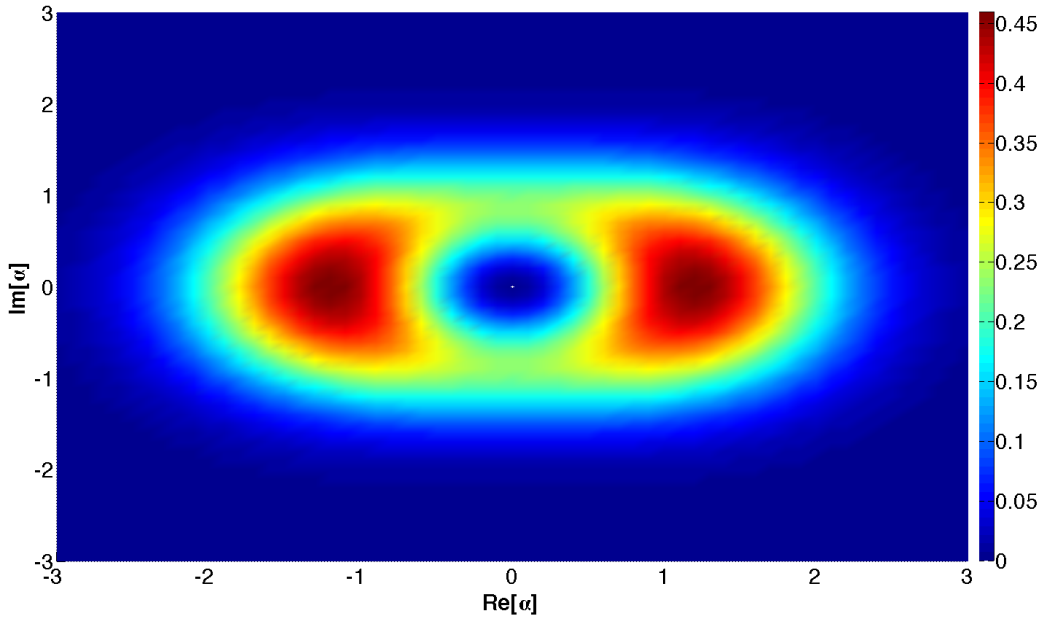

Figure 1.3: This figure shows the Husimi Q function for an odd Schrödinger cat state with $|\alpha| = 1$. The double peaked structure of the distribution, corresponding to the two coherent state components centred at α and $-\alpha$, is evident.

Chapter 2

Theory of Josephson Photomultipliers: Optimal Working Conditions and Back Action

2.1 Overview

The research presented in this chapter was done in collaboration with my supervisor Frank Wilhelm, as well as Emily Pritchett, Seth Merkel and Deanna Pineau. This chapter consists of the written record of this research, which has been accepted for publication, and can be found at (arXiv:1206.0360). The contents of this chapter were written in collaboration with the above mentioned, and in particular sections 2.2, and 2.7 were largely written or heavily edited by Frank Wilhelm and Emily Pritchett.

Section 2.4 presents a very general overview of the computational method used to simulate the evolution of a coupled JPM and microwave cavity. For a more detailed explanation of this method, as well as other methods initially applied to the problem, see appendix A.

2.2 Introduction

Recently, many of the benchmark experiments of cavity quantum electrodynamics (QED) [7, 8, 3, 9] have been reproduced with superconducting circuits [10, 11, 12, 13, 14, 15, 16, 17], which operate in the quantum regime via exchange of microwave-frequency excitations [18, 19, 20, 21, 22]. On these circuits, nonlinear devices couple to the microwave-frequency modes of transmission lines via ordinary circuit devices such as capacitors or inductors [23, 24, 25], much as atoms couple to modes of a resonant electromagnetic cavity. A fixed number of these artificial atoms can be fabricated in a given circuit, and their energy levels and interactions are tunable both at fabrication and during the course of an experiment. For these reasons, circuit-QED (cQED) receives attention both as a possible platform for scalable, universal quantum computing [26, 27] and for its ability to operate in regimes inaccessible by atomic cavity-QED [28, 29, 30, 31, 32, 33, 34, 35].

While many of the tools available in cavity-QED are straightforward to reproduce in the circuit analogue, the detection of single microwave-frequency photons proves challenging. Traditionally, the lower cutoff frequency of photon counters is determined by the work function or band gap of a certain material, which is at a minimum in the infrared range for stable materials. There are currently a few theoretical proposals for the construction of microwave photon counters [36, 37, 38], and recently it was demonstrated experimentally that a current-biased Josephson junction [39, 40, 41, 42, 43, 44] can be used to count microwave photons [45]. We refer to such a device as a Josephson photomultiplier (JPM), distinguishing it from a phase qubit [46, 47] because the optimal operating conditions for photon detection are different than those required for storage of quantum information.

Photon counters should be contrasted with amplifiers. While the former are sensitive to the intensity of the incoming radiation but not to the phase,

the latter amplify the quadratures of the signal. Even though commercial microwave amplifiers operate far from the quantum limit, researchers have recently demonstrated single-photon sensitivity in phase-preserving microwave amplification [48, 49, 50, 51, 52, 53, 54, 55, 56]. By contrast, phase-insensitive photon counters have proven useful in quantum optics for reconstruction of the quantum state of light as, for example, in homodyne tomography. Workarounds to microwave photon counting based on linear amplification have been formulated [57, 58] and demonstrated [59, 60, 61].

As microwave photon counters, JPMs have an important application in efficient quantum state tomography of microwave photon states. Given that measurement by a JPM provides only limited information – a click indicates the presence of one or more photons – the post-measurement state still contains coherent information about the initial state. Following the idea of quantum regression this post-measurement state is connected to the pre-measurement state by back action operators. Hence, if the back action operators are known, repeated measurements on a chain of post-measurement states can provide additional information about the original state.

In this chapter, we theoretically model the back action of the proposed JPM, obtaining the precise relation between pre- and post-measurement states. This knowledge may allow efficient state tomography [62, 63] including, for example, adaptive techniques [64], or any other application requiring knowledge of the post-measurement state. We note that our results are based on a very abstract model and thus extend to other detection schemes whereby a quantum two-level system strongly couples to a resonant linear oscillator, so long as the observable detection event involves incoherent tunnelling from an energy level of the two-level system (and not the oscillator). For example, this situation applies to some setups in atomic cavity QED. We include realistic estimations of the energy dissipation and dephasing rates of a JPM, showing that operating the JPM in the regime of

fast dephasing (short T_2) reduces the amount of dephasing incurred during measurement, and is thus advantageous.

In the following section, we discuss our model for the JPM. In section 2.4, we discuss the formalism of process tomography used to characterize the back action of the JPM. In section 2.5, we give the back action both numerically and analytically in a variety of instructive and/or experimentally relevant regimes. In section 2.6, we discuss how to extract the operating regime of the JPM by simple tests with coherent light. Finally, in section 2.7, we discuss the optimal working conditions of the JPM for the purpose of cavity state reconstruction.

2.3 Physical Model

A JPM consists of a current-biased Josephson junction (CBJJ) [39, 40, 41, 42, 43, 44] capacitively coupled to the microwave cavity of interest. The potential energy of a JPM , shown in figure 2.1, is

$$U(\phi) = -I_c \frac{\Phi_0}{2\pi} \cos\phi - I_b \frac{\Phi_0}{2\pi} \phi \tag{2.1}$$

where I_c is the critical current of the junction externally biased by current I_b, ϕ is the superconducting phase difference across the junction, and $\Phi_0 = \frac{\hbar}{2e}$ is the magnetic flux quantum. We consider a junction biased such that the potential well contains only a few meta-stable states. All of these states can tunnel incoherently out of the potential well, but due to the exponential relationship between tunnelling rate and barrier height, the tunnelling rate for higher energy states is several orders of magnitude higher than that for the ground state (see chapter 1.2 for further information on phase qubits). Note that, in analogy to the phase qubit, the current source can be replaced by a large, flux-biased superconducting loop [65, 47].

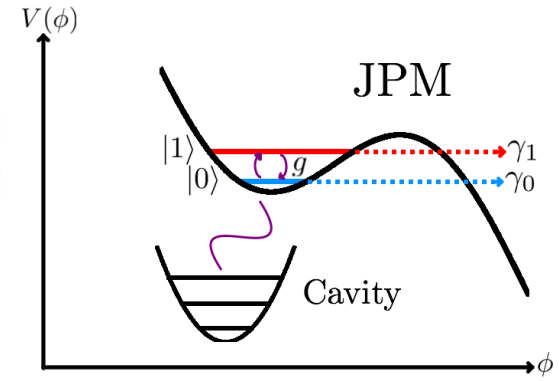

Figure 2.1: This figure is a diagrammatic representation of the potential energy of a JPM as a function of the superconducting phase difference, and shows the interaction with a microwave cavity.

Photon detection relies on an incident microwave photon to transition the JPM to its first excited state. This transition is enhanced by pulsing the bias current, bringing the energy level splitting of the ground and first excited state of the JPM on- or near-resonant with the microwave cavity. Once the JPM reaches its excited state, it tunnels more rapidly out of the metastable state. This tunnelling process is incoherent, resulting in a measurable voltage pulse in the circuit that is interpreted as the detection of a single photon [41, 42, 44, 43, 45]. By comparison, a related method of cavity state reconstruction determines the number of cavity photons present by the frequency of coherent oscillation between the cavity and a phase qubit [29].

We assume that the JPM and cavity states are initially separable with the JPM in the lowest energy metastable state. Physically, this means that the JPM and microwave cavity must be brought on resonance adiabatically with respect to the JPM's internal evolution, but non-adiabatically with respect to the cavity-JPM interaction. We describe the full system's Hilbert space with tensor products of single mode cavity eigenstates and three detector states, $\{|0\rangle_{\mathrm{d}}, |1\rangle_{\mathrm{d}}, |m\rangle_{\mathrm{d}}\}$. The states $|0\rangle_{\mathrm{d}}$ and $|1\rangle_{\mathrm{d}}$ correspond to the ground

and first excited metastable states of the JPM, while the measured state $|m\rangle_{\mathrm{d}}$ is an amalgamation of the many possible states that the JPM can tunnel into incoherently, producing an observable output voltage.

It is possible to ignore the energy level structure of the states outside the logical potential well (and consider only a single state $|m\rangle_{\mathrm{d}}$) provided that energy exchange between the logical well and these external states is a one way process. This is built into our model, as the JPM is allowed to tunnel only incoherently into the measured state, a process described by the Lindblad operator 2.5, and there is no coherent energy exchange between the logical states and the measured state (the operators $\hat{\sigma}^{\pm}$ do not couple the logical states to the measured state). When these conditions are met, the details of the constituent states of the measured state will have no effect on the dynamics of the JPM.

The coherent interaction between the cavity and the JPM as well as the relevant incoherent processes (for example, tunnelling into the measured state, dephasing, and relaxation) are described by the quantum master equation

$$\dot{\xi}(t) = \hat{S}[\xi(t)] = -i[\hat{H}, \xi(t)] + \sum_{\mu} \left(\hat{J}_{\mu} \xi(t) \hat{J}_{\mu}^{\dagger} - \frac{1}{2} \{ \hat{J}_{\mu}^{\dagger} \hat{J}_{\mu}, \xi(t) \} \right) \tag{2.2}$$

where $\xi(t)$ is the cavity-JPM system's density matrix (see section 1.3 for further information on master equations). Here H is the Jaynes-Cummings interaction (on resonance assumed)

$$\hat{H} \equiv g(\hat{a}^{\dagger} \hat{\sigma}^{-} + \hat{a} \hat{\sigma}^{+}) \tag{2.3}$$

where $\hat{a}$ and $\hat{a}^{\dagger}$ are the lowering and raising operator associated with the cavity mode, $\hat{\sigma}^{\pm}$ are the lowering and raising operators between the states $|0\rangle_{\mathrm{d}}$ and $|1\rangle_{\mathrm{d}}$, and g is the coupling strength between the cavity and the JPM. Note that this Hamiltonian conserves total excitation number and

does not couple photons coherently to the measured state, which simplifies the following analysis.

A set of Linblad operators $\{\hat{J}_\mu\}$ describe the relavent incoherent processes.

$$\hat{J}_1 \equiv \sqrt{\gamma_1}(\hat{\mathbb{I}}_\mathrm{c} \otimes |\mathrm{m}\rangle \langle 1|_\mathrm{d}) \tag{2.4}$$

describes incoherent tunnelling out of the excited metastable state leaving one less excitation in the cavity, and thus corresponding to photon measurement. Tunnelling out of the metastable ground state is described by

$$\hat{J}_0 \equiv \sqrt{\gamma_0}(\hat{\mathbb{I}}_\mathrm{c} \otimes |\mathrm{m}\rangle \langle 0|_\mathrm{d}) \tag{2.5}$$

where γ_0 is the effective dark count rate since a measurement signal is produced without changing the number of excitations in the cavity. We also include Linblad operators to describe pure dephasing of the JPM over characteristic time T_2

$$\hat{J}_2 \equiv \frac{1}{\sqrt{T_2}}(\hat{\mathbb{I}}_\mathrm{c} \otimes |1\rangle \langle 1|_\mathrm{d}) \tag{2.6}$$

and energy relaxation from the excited state to the ground state of the JPM over characteristic time T_1

$$\hat{J}_3 \equiv \frac{1}{\sqrt{T_1}}(\hat{\mathbb{I}}_\mathrm{c} \otimes |0\rangle \langle 1|_\mathrm{d}). \tag{2.7}$$

In general the cavity decoheres as well [66, 67], but this happens slowly compared to other relevant timescales.

2.4 Process Tomography

For tomography of the process of cavity state measurement by a JPM, we calculate the Liouville supermatrix $\mathcal{T}(t)$ generated by

$$\mathcal{S} \equiv -i\left(\hat{H} \otimes \hat{\mathbb{I}} - \hat{\mathbb{I}} \otimes \hat{H}\right) + \sum_\mu \left(\hat{J}_\mu \otimes \hat{J}_\mu^* - \frac{1}{2}\hat{J}_\mu^\dagger \hat{J}_\mu \otimes \hat{\mathbb{I}} - \frac{1}{2}\hat{\mathbb{I}} \otimes (\hat{J}_\mu^\dagger \hat{J}_\mu)^*\right),$$

which transforms an arbitrary, vectorized initial cavity-JPM state to the solution of (2.2):

$$\vec{\xi}(t) = \mathcal{T}(t)\vec{\xi}(0) = e^{\mathcal{S}t}\vec{\xi}(0). \tag{2.8}$$

We then transform the Liouville supermatrix into the more commonly used χ-matrix representation [1, 68], which, for a given basis $\{\hat{E}_\mu\}_{\mu=0}^{N^2-1}$ of operator space $\mathcal{L}(\mathcal{H})$, satisfies

$$\xi(t) = \sum_{\mu\nu=0}^{N^2-1} \chi_{\mu\nu}(t)\hat{E}_\mu\xi(0)\hat{E}_\nu^\dagger. \tag{2.9}$$

In the standard basis, $E_{\mu(\alpha,\beta)} \equiv |\alpha\rangle\langle\beta|$ where $\mu(\alpha,\beta) \equiv (N \times \alpha) + \beta$ and $\{|\alpha\rangle\}_{\alpha=0}^{N-1}$ is an eigenbasis of the full system's noninteracting Hamiltonian, the χ-matrix elements are simply

$$\chi_{\mu(\alpha,\beta)\nu(\gamma,\delta)}(t) \equiv \chi_{\alpha\beta\gamma\delta}(t) = \langle\alpha|\left(e^{\mathcal{S}t}|\beta\rangle\langle\delta|\right)|\gamma\rangle \tag{2.10}$$

and can be obtained by a permutation of the Liouville supermatrix elements: $\chi_{\alpha\beta\gamma\delta} = T_{\alpha\gamma\beta\delta}$. In all calculations, we assume an initial state of the form

$$\xi(0) = \rho_{\mathrm{c}}(0) \otimes |0\rangle\langle 0|_{\mathrm{d}}, \tag{2.11}$$

a product state of the initial cavity state, $\rho_{\mathrm{c}}(0)$, and the lowest energy metastable state of the JPM. Preparation of this factorized state has already been described earlier (section 2.3).

We are interested in the back action of the JPM onto the cavity state conditioned on measurement outcome $s \in \{0, 1, \mathrm{m}\}$,

$$\rho_{\mathrm{c}}^s(t) = \frac{\langle s|e^{\hat{S}t}\xi(0)|s\rangle_{\mathrm{d}}}{P^s(t)}, \tag{2.12}$$

where $P^s(t)$ normalizes the cavity state by the probability of obtaining JPM final state $|s\rangle_{\mathrm{d}}$. Only incoherent tunnelling into the measurement state is

allowed by our model, so no coherent superposition between the measured and non-measured state is possible. Therefore, $\rho_{\mathrm{c}}^{s=\mathrm{m}}$ gives the cavity state after detection of a photon, and in the case that no photon is detected, the cavity will be in a mixture of the states with $s = 0, 1$. Each outcome is completely described by an off-diagonal $d_{\mathrm{cav}}^2 \times d_{\mathrm{cav}}^2$ block of the full χ-matrix, which is by itself a valid χ-matrix of the isolated cavity. We label these reduced χ-matrices χ^s, which completely describe the evolution of an arbitrary initial state $\rho_{\mathrm{c}}(0)$, in the case of measurement outcome s.

2.5 Analytical and Numerical Solutions for the χ-Matrix

2.5.1 No Tunnelling Model

To understand the back action of photon detection, we first consider a simpler model where there are no incoherent processes, and measurement of a photon corresponds to projecting the JPM onto its metastable excited state $|1\rangle_{\mathrm{d}}$ (rather than $|\mathrm{m}\rangle_{\mathrm{d}}$). In this model, eq. (2.2) reduces to $\dot{\xi}(t) = -i[\hat{H}, \xi(t)]$, and the cavity conditioned on measurement outcome s at time t can be expressed in terms of a single time-dependent back action operator $\hat{B}^s(t)$ acting only on the Hilbert space of the cavity:

$$\rho_{\mathrm{c}}^s(t) = \frac{\hat{B}^s(t)\xi(0)\hat{B}^s(t)^\dagger}{P^s(t)}. \tag{2.13}$$

Furthermore, in this model, the $\hat{B}^s(t)$ are straightforward to calculate explicitly:

$$\hat{B}^1(t) \equiv \langle 1|\xi(t)|0\rangle_{\mathrm{d}} = -i\sum_{n=1}^{\infty} \sin(gt\sqrt{n})\, |n-1\rangle \langle n|_{\mathrm{c}} \tag{2.14}$$

$$\hat{B}^0(t) \equiv \langle 0|\xi(t)|0\rangle_{\mathrm{d}} = \sum_{n=0}^{\infty} \cos(gt\sqrt{n})\, |n\rangle \langle n|_{\mathrm{c}}\,. \tag{2.15}$$

The cavity is initialized in a superposition of n-photon Fock states, and when only coherent cavity-JPM interaction is included, each n-photon Fock state in superposition will exchange a single excitation with the JPM at a Rabi frequency $g\sqrt{n}$. Measurement projects the detector onto $|0\rangle_{\rm d}$ or $|1\rangle_{\rm d}$, modifying the cavity with back action $\hat{B}^0(t)$ or $\hat{B}^1(t)$, respectively. From these operators we obtain the average detection probability

$$P^1(t) \;=\; \left\langle \hat{B}^{1\dagger}(t)\hat{B}^1(t)\right\rangle_0 = \sum_n P_n^1(t)\,\langle n|\,\rho_c(0)\,|n\rangle \tag{2.16}$$

where $P_n^1(t) \equiv \sin^2(gt\sqrt{n})$ is the detection probability when the n-photon Fock state is initially prepared.

It is possible, by averaging over repeated measurements at increasing time intervals, to distinguish Fock states and incoherent mixtures of Fock states by Fourier transforming the average detection probability $P^1(t)$, as was demonstrated in ref. [69]; however, more sophisticated state tomography is required for resolving superpositions of Fock states. One approach is to displace the cavity state and reconstruct a convenient phase space description of its initial state, repeating measurements and averaging at every point in phase space that is resolved [29]. Here we look for a quantum description of the measured cavity state so that repeated measurements on a single input state can be used for a more efficient state tomography.

From the behavior of (2.14),

$$\hat{B}^1 = (-igt)\hat{a} + \mathcal{O}(\sqrt{n}gt)^3, \tag{2.17}$$

we can see that at short-times (and finite n), the measurement back action is proportional to the photon lowering operator. Furthermore, at short times, different Fock states can be distinguished by their tunnelling rate into the detector, $\Gamma_n \equiv g^2 n$. However, at longer times $t \gtrsim t_n \equiv 1/g\sqrt{n}$, the oscillations from different Fock states become out of phase and difficult to

distinguish. This effect is described by the correction to the $\hat{a}$ operator in (2.17).

We note that back action is well-described by the lowering operator when the interaction times t_n (for the largest occupied n) are the largest time scales of the system. This happens, for example, in the free photon regime where coupling strengths are very weak [70]. Also, we will later show that in the richer model where detection corresponds to tunnelling out of the $\langle 1|_{\mathrm{d}}$ at the rate γ_1, the lowering operator is a good approximation to the back action for times shorter than the excited state tunnelling time γ_1^{-1}. To detect low-energy microwave photons, however, we need measurement times long compared to t_{n} and γ_1^{-1}, and corrections to the lowering operator become important to fully understand the back action associated with photon detection.

2.5.2 Full (Tunnelling) Model

In the full model, a detection event corresponds to the detector incoherently tunnelling to the 'measurement' state $|\mathrm{m}\rangle_{\mathrm{d}}$, which corresponds to the JPM observably tunnelling from a metastable state to a near continuum of levels. The JPM does not reset to its initial state on a time scale comparable to the measurement interval and therefore can not resolve the total number of photons present in the cavity, only whether there is at least one present. Therefore, we do not expect the measurement back action on the cavity to be exactly the photon annihilation operator, but rather an operator of the form

$$\hat{B}_{\mathrm{m}} = \sum_{n=1}^{\infty} |n-1\rangle\langle n|. \tag{2.18}$$

which we refer to as the subtraction operator. We note that this back action can be used to separate the number-dependent part of the annihilation

operator,

$$\hat{a} \equiv \hat{B}_{\mathrm{m}} \hat{N}^{1/2}, \tag{2.19}$$

and was thus considered as the exponential of a quantum phase operator by Susskind and Glogower [71], but a currently more accepted unitary version was proposed by Pegg and Barnett [72].

While in the no-tunnelling model the measurement back action reflects undamped Rabi oscillations between the cavity and JPM, we expect these oscillations to be damped by incoherent tunnelling out of the metastable states of the JPM so that, when averaged over an entire measurement interval, the back action has the form of (2.18). Transitions occur from $|n\rangle$ to $|n-1\rangle$ photon Fock states, with no preference on the number n of photons originally present. However, because the *initial* tunnelling rate depends on the number of photons present, and it takes time for this averaging effect to occur, we expect that for measurement intervals short compared to t_n and γ_1^{-1} the back action will more closely resemble that of the usual photon-number resolving annihilation operator.

To understand the distinguishing signatures of $\hat{a}$ and $\hat{B}_{\mathrm{m}}$ in the framework of process tomography, it is instructive to examine the χ^1 matrices corresponding to each. Both will have

$$\chi^1_{j-1jk-1k} \equiv \beta_{jk} \quad \forall j,k \in \{1,...,N-1\} \tag{2.20}$$

non-zero, corresponding to superpositions of $|j\rangle$ and $|k\rangle$ photons transitioning to $|j-1\rangle$ and $|k-1\rangle$ photons. For a good photon detector, the number of excitation in a given Fock state is decreased by exactly one, therefore all other elements of χ^1 are zero. When the back action operator is $\hat{a}$,

$$\beta_{jk} = \sqrt{jk}, \tag{2.21}$$

while for $\hat{B}_{\mathrm{m}}$,

$$\beta_{jk} = 1 \tag{2.22}$$

for all values of $j, k \in \{1, ..., N-1\}$. In the following section, we numerically study the time-dependence of the β_{jk} in our full physical model, using the values of β_{jk} for known examples of back action models as a point of reference.

2.5.3 Numerical Simulations for the χ^1 Matrix

Bare JPM

Here we present the χ^1-matrix elements numerically generated using the Liouville supermatrix approach, first in the case of a bare detector experiencing no dark counts, dephasing, or energy dissipation ($\gamma_0 = 0$ and $T_1 = T_2 = \infty$). In this case, the χ^1-matrix has the same nonzero elements as those for $\hat{a}$ and $\hat{B}_{\mathrm{m}}$, labelled above as β_{jk}.

The β_{jk} are plotted as a function of total measurement time (t_m) in figure 2.2 for $j, k \in \{1, 2, 3, 4\}$. As is demonstrated clearly by the diagonal $\alpha_j \equiv \beta_{jj}$ plotted in figure 2.2(a), the χ^1-matrix elements show oscillatory behaviour at n-dependent frequencies, as in equation (2.14), $g\sqrt{n}$. Similarly, the off-diagonal elements also show oscillatory behaviour, as can be seen in figure 2.2(b).

In the long time limit, the diagonal elements all tend to unity as expected for a back action resembling the subtraction operator, however, the off-diagonal elements do not. This additional dephasing can be explained by the uncertainty in time of the switching event, which is of the order γ_1^{-1}. As the phase of the off-diagonal matrix elements precesses with frequencies proportional to g, this uncertainty gives a spread of the phase of size g/γ_1. We will later see how decoherence reduces this uncertainty, thus reducing the amount of dephasing incurred by measurement.

Pure Dephasing

We now consider a JPM that experiences pure dephasing between its ground and excited states, as would be described by a master equation including the Lindblad operator $\hat{J}_2$ of equation (2.6). In this case, the χ^1-matrix has the same non-zero elements as that for the bare detector since the selection rules imposed by the conservation of excitation number are still valid. The bare detector and pure dephasing χ^1-matrix elements are compared in figure 2.3, where the dephasing time has been chosen such that $\frac{1}{T_2} = 10\ \gamma_1$, deep in the strong dephasing regime.

As can be seen in figure 2.3, decreasing the value of T_2 has multiple effects. On the one hand, the photon transfer from the cavity into the detector is slowed down by decreasing T_2, so at short time the χ^1-matrix elements are smaller. Also, the coherent oscillations are damped as T_2 has the effect of turning the coherent tunnelling between the cavity and the JPM into an incoherent process, similar to the crossover from strong coupling cavity QED to the Purcell regime [3]. In fact, a phase Purcell effect has been discussed in [73, 74]. This affects both the diagonal and off-diagonal χ^1-matrix elements.

Once the photon transfer efficiency is no longer a limiting factor, the asymptotic limit of the diagonal χ^1-matrix elements is not affected by T_2. The off-diagonal elements saturate to a value that is set by measurement-induced dephasing which is lowered by short T_2 (as seen in figure 2.4(a)). This reduction in measurement-induced dephasing is due to the fact that T_2 turns the coherent tunnelling between cavity and JPM into an incoherent process, and thus reduces the phase precession of the off-diagonal elements and with it the uncertainty of these phases at the moment of measurement. Although the amount of dephasing decreases with decreasing T_2, the total measurement time required for the χ-matrix elements to reach their asymptotic value increases, as shown in figure 2.4(b).

To further illuminate the effect of pure dephasing on a JPM we look at the probability of detection for a coherent state input and a one-photon Fock state input. In figure 2.5, we see that for both input states, dephasing suppresses the oscillations in detection probability exhibited by the bare JPM. These oscillations result from coherent excitation swapping (Rabi-type oscillations) between the cavity and JPM, and superpositions of an excitation in the JPM and in the resonator are subject to dephasing processes in the JPM. This pure dephasing turns coherent JPM-cavity oscillations into incoherent resonant tunnelling.

In the long time limit, both the dephased and bare JPM detect a photon with the same probability. Thus, it is not necessary to aim at long T_2 values for a JPM as one would for a phase qubit [46, 47]. On the contrary, we see that the dephasing incurred by measurement is smaller at short T_2, rendering it advantageous. A more detailed discussion about T_2 as an engineering parameter will be given in the end of the paper.

Energy Relaxation of the JPM

We consider a JPM experiencing energy dissipation, as described by a master equation including the Lindblad operator $\hat{J}_3$ of equation (2.7). In this situation, the JPM will also experience associated dephasing on a timescale $T_2 = 2T_1$. The χ^1-matrix of a dissipating JPM has additional non-zero elements (in addition to the β_{jk}) attributed to a change of total excitation number. As the JPM can lose photons into an external heat bath, it is possible that multiple photons from the cavity might excite the JPM before a detection event occurs. The nonzero χ^1-matrix elements are of the form

$$\beta_{jk}^{(r)} \equiv \chi^1_{j-1j+rk-1k+r}, \tag{2.23}$$

corresponding to the loss of integer $0 < r < \min\{k, j\}$ photons before detection. $\beta_{jk}^{(0)} = \beta_{jk}$ from the previous sections, and the diagonal elements

are relabeled $\alpha_j^{(r)} \equiv \beta_{jj}^{(r)}$.

In figure 2.6 we compare the $\alpha_j^{(0)}$ for an energy relaxation timescale of $\frac{1}{T_1} = \gamma_1$ to the α_j of a detector with infinite T_1. Unlike the case of pure dephasing, energy loss from the JPM reduces the asymptotic value of these χ^1-matrix elements. We also note that the off-diagonal $\beta_{jk}^{(0)}$ evolve exactly like those of a JPM experiencing pure dephasing, as shown in figure 2.3(b), but with an effective T_2 of $2T_1$. The diagonal χ^1-matrix elements $\alpha_j^{(r)}$ are shown in figure 2.7 for different values of r.

As in the case of pure dephasing, it is instructive to see the effect of energy relaxation on the probability of photon detection for specific input states. Figure 2.8 shows the detection probability as a function of time for both coherent states and one photon Fock states. The short time oscillatory behaviour of the bare JPM detection probability is strongly suppressed by energy relaxation because of the effective dephasing rate $T_2 = 2T_1$. In addition to this dephasing effect, the detection probability of a JPM experiencing energy relaxation asymptotes more quickly to a smaller value than that of a bare JPM.

A plot of the asymptotic value of detection probability as a function of energy relaxation rate, T_1^{-1}, is shown in figure 2.9 for a one photon Fock state input. The JPM experiences competing decay channels (energy relaxation and incoherent tunnelling into the measured state), only one of which results in photon detection. This reduces the time required for the probability to reach its asymptotic value as well as the overall probability that a detection will occur. In the case where these two decay rates are equal, the single photon detection probability will be exactly half of what it would be for a bare detector, as seen in figure 2.8.

Dark Counts

The final modification of interest is tunnelling out of the $|0\rangle_{\mathrm{d}}$ state, a detection event which does not change the number or excitations in the cavity and is therefore considered a dark count. This is described by a master equation including the Lindblad operator $\hat{J}_0$ of equation (2.5). The χ^1-matrix has, in addition to all the non-zero elements of the bare JPM, additional non-zero elements

$$\chi^1_{jjkk} \neq 0 \; \forall \; j,k \in \{0,1,..N-1\}. \tag{2.24}$$

These elements correspond to detection events that occur without changing the k-photon Fock state in the cavity. The JPM experiencing dark counts will appear to have a higher probability of photon detection than a bare JPM; however, this increased probability is due to false detections. Dark counts limit the detector contrast by the ratio between true and false detections.

We are not aware of any simple way to correct for all the effects of dark counts on detection probability without a priori information about the detected state; however, by the appropriate choice of experimental parameters, the dark count rate can be made to be quite small for a JPM – as much as 2 to 3 orders of magnitude smaller than the excited state tunnelling rate [45]. It is therefore not unreasonable to simulate a dark count rate of 5 % of the excited state tunnelling rate as a conservative estimate.

Figure 2.10 shows the detection probability for a one-photon Fock state input with a 5% dark count rate, which is very similar to that of a bare JPM; however, for a coherent state with $\langle n \rangle = |\alpha|^2 = 1$, dark counts significantly change the detection probability since the coherent state has a significant vacuum component. This deviation decreases as $|\alpha|$ of the coherent state increases.

2.5.4 Analytical Solutions in the Low T_2 Regime

While a full analytic solution of the system's master equation does not promise more illumination than the numerical results presented above, here we obtain the short T_2 behavior of the detector by making appropriate approximations. We begin by defining the block cavity matrix

$$\rho_{ij}(t) \equiv \langle i|_{\mathrm{d}}\, \xi(t)\, |j\rangle_{\mathrm{d}} \tag{2.25}$$

where $|i\rangle_{\mathrm{d}} \equiv \mathbb{I}_{\mathrm{c}} \otimes |i\rangle_{\mathrm{d}}$ project $\xi(t)$ on the basis states of the noninteracting JPM. We are interested in the unrenormalized state of the cavity after photon detection, which corresponds to the cavity state $\rho_{mm}(t)$. From the full master equation, it can be shown that

$$\dot{\rho}_{\mathrm{mm}}(t) = \langle m|_{\mathrm{d}}\, e^{St} \xi(0)\, |m\rangle_{\mathrm{d}} = \gamma_1 \rho_{11}(t) \tag{2.26}$$

in the case that $\gamma_0 = 0$. Thus, the instantaneous time evolution of ρ_{mm} depends only on ρ_{11}, the unnormalized state conditioned on the JPM being in the excited state.

The time evolution of ρ_{11} is governed by a system of four first-order operator differential equations:

$$\begin{aligned}
\dot{\rho}_{11} &= ig\left(\rho_{10}\hat{a}^\dagger - \hat{a}\rho_{01}\right) - \gamma_1\rho_{11} \\
\dot{\rho}_{00} &= ig\left(\rho_{01}\hat{a} - \hat{a}^\dagger\rho_{10}\right) \\
\dot{\rho}_{01} &= ig\left(\rho_{00}\hat{a}^\dagger - \hat{a}^\dagger\rho_{11}\right) - \frac{\gamma_1+\kappa_2}{2}\rho_{01} \\
\dot{\rho}_{10} &= ig\left(\rho_{11}\hat{a} - \hat{a}\rho_{00}\right) - \frac{\gamma_1+\kappa_2}{2}\rho_{10}
\end{aligned} \tag{2.27}$$

where we have introduced the pure dephasing rate $\kappa_2 = \frac{1}{T_2}$ for notational convenience. This system can be reduced to a single fourth order operator differential equation in terms of $\rho_{11}(t)$, as shown in equation (B.1).

Now for simplicity, we consider the occupation probability of the cavity state $|n\rangle\langle n|_c$ given that a photon detection has occurred,

$$P_n(t) \equiv \int_0^t \langle n|_c \, \dot{\rho}_{mm}(t') \, |n\rangle_c \, dt', \tag{2.28}$$

which from (2.26) can be expressed as

$$P_n(t) = \gamma_1 \int_0^t x(t')dt', \tag{2.29}$$

where we have defined the matrix element

$$x(t) \equiv \langle n|_c \, \rho_{11}(t) \, |n\rangle_c \, . \tag{2.30}$$

The full master equation reduces to the fourth order differential equation in $x(t)$, given in (B.2).

Before attempting to solve the somewhat cumbersome equation (B.2), we make the simplifying assumption that T_2 is the smallest time scale of the system's evolution, and keep only the highest order terms in $\frac{g}{\kappa_2}, \frac{\gamma_1}{\kappa_2} \ll 1$. This gives

$$x^{(4)} + \kappa_2 x^{(3)} + \frac{1}{4}\kappa_2^2 x^{(2)} + \frac{1}{4}\gamma_1\kappa_2^2 x^{(1)} + \kappa_2 g^2 \gamma_1 (1+n)x = 0, \tag{2.31}$$

which can be solved with Laplace transforms. Defining $X(s) \equiv \mathcal{L}[x(t)]$, equation (2.31) in the Laplace domain is

$$\begin{aligned} X(s) &= 2g^2(n+1)x_0 \left(s + \frac{\kappa_2 - 3\gamma_1}{2}\right) \\ &\times \left(s^4 + \kappa_2 s^3 + \frac{1}{4}(\kappa_2^2 s^2 + \kappa_2^2 \gamma_1 s) + \kappa_2 g^2 \gamma_1 (n+1)\right)^{-1} \end{aligned} \tag{2.32}$$

where $x_0 \equiv x(0) = \langle n|_c \, \rho_{11}(0) \, |n\rangle_c$.

While still very general and valid for all input states, equation (2.32) is still somewhat unwieldy. However, in the limit of short T_2, we can assume that coherent oscillations between the cavity and JPM become incoherent tunnelling. Defining $\Gamma_{\alpha,\beta\to\delta,\gamma}$ to be the tunnelling rate from state $|\alpha\rangle_{\mathrm{c}} \otimes |\beta\rangle_{\mathrm{d}}$ to state $|\gamma\rangle_{\mathrm{c}}| \otimes |\delta\rangle_{\mathrm{d}}$, we take

$$\begin{aligned} \Gamma_{\mathrm{n},0\to\mathrm{n}-1,1} &= \Gamma_{\mathrm{n}-1,1\to\mathrm{n},0} = 4ng^2T_2 \\ \Gamma_{\mathrm{n},1\to\mathrm{n},\mathrm{m}} &= \gamma_1 \end{aligned} \tag{2.33}$$

Here $\Gamma_{\mathrm{n},0\to\mathrm{n}-1,1}$ is the incoherent tunnelling rate from the cavity into the JPM when n photons are present, and $\Gamma_{\mathrm{n}-1,1\to\mathrm{n},0}$ the rate for the inverse process. Both rates are broadened by short T_2, which can be understood in terms of the Purcell effect. If we consider only Fock state inputs, the occupation probabilities

$$P_{n,\mathrm{j}}(t) \equiv \langle n|_{\mathrm{c}}\, \rho_{\mathrm{jj}}(t)\, |n\rangle_{\mathrm{c}} \quad \mathrm{j} \in \{0, 1, \mathrm{m}\} \tag{2.34}$$

of the cavity being in the n-photon Fock state and the detector being in state $|\mathrm{j}\rangle_{\mathrm{d}}$ obey the Pauli master equation. Using the rate in (2.33), this simplifies to

$$\begin{aligned} \dot{P}_{n,0} &= n\gamma_2 \left(P_{n-1,1} - P_{n,0}\right) \\ \dot{P}_{n,1} &= (n+1)\gamma_2 \left(P_{n+1,0} - P_{n,1}\right) - \gamma_1 P_{n,1} \\ \dot{P}_{n,\mathrm{m}} &= \gamma_1 P_{n,1} \end{aligned} \tag{2.35}$$

where $\gamma_2 \equiv (2g)^2 T_2 \equiv (2g)^2/\kappa_2$. For an n-photon Fock state input, $P_{n,0}(0) = 1$ and the total number of excitations in the system is fixed to n, so at later times only $P_{n,0}$, $P_{n-1,1}$ and $P_{n-1,\mathrm{m}}$ are nonzero.

The equations (2.35) can be solved to find the detection probability as a function of time (the details of this are shown in Appendix B, giving

$$P_{n,\mathrm{m}}(t) = 1 + \frac{\gamma_1\gamma_2 n}{(s_+ - s_-)} \left(\frac{e^{s_+ t}}{s_+} - \frac{e^{s_- t}}{s_-}\right) \tag{2.36}$$

where

$$s_{\pm} = \frac{1}{2}\left(-\gamma_1 - 2\gamma_2 n \pm \sqrt{\gamma_1^2 + 4\gamma_2^2 n^2}\right). \tag{2.37}$$

We can distinguish two regimes for this solution. In the tunnelling-limited regime, $\gamma_1 \ll \gamma_2 n$ we find $s_+ \simeq -\gamma_1/2$ and $s_- \simeq -2\gamma_2 n$ and have

$$P_{n,m}(t) = 1 - e^{-\gamma_1 t/2} + O(\gamma_1/\gamma_2 n) \tag{2.38}$$

In the opposite regime, photon capture is the slower, limiting process ($\gamma_1 \gg \gamma_2 n$). In this regime, $s_+ = -\gamma_2 n$ and $s_- = -\gamma_1 - \gamma_2 n$ and we find

$$P_{n,m} = 1 - e^{-\gamma_2 n t} + O(\gamma_2 n/\gamma_1) \tag{2.39}$$

The differences between these regimes is evident in figure 3(a); with added dephasing, $\gamma_1 \gg \gamma_2 n$, and the detection probabilities $P_{n,m} = \alpha_n$ reach their asymptotic values more slowly and with n-dependence. Without the added dephasing, $\gamma_1 \ll \gamma_2 n$, the rate at which the detection probabilities reach their asymptotic value is determined by γ_1, and independent of n.

Equation (2.36) agrees to a high degree of accuracy with the numerical simulations for a JPM experiencing pure dephasing with a very short dephasing time, T_2. As can be seen in figure 2.11(a) for one and two photon Fock states, this agreement occurs at all times. Interestingly, even at longer T_2 the analytical solution is still a good approximation to the numerical simulation. By design, the analytical solution ignores coherent oscillations between the cavity and the JPM, and so in the long T_2 regime the analytical solution does not display the oscillatory behaviour of the numerical solution, but instead describes its average behavior. This can be seen in figure 2.11(b), for one and two photon Fock state inputs.

2.6 Coherent State Test

In this section, we propose a test to determine whether a given JPM's back action is closer to the lowering operator or the subtraction operator in order to correctly characterize the JPM. Additionally, such a test would allow us to examine the effects of energy relaxation and pure dephasing on the time evolution of the back action.

2.6.1 The Dependence of Detection Probability on Coherent State Power

Consider a coherent state expressed in the Fock basis, $|\alpha\rangle = e^{-\frac{|\alpha|^2}{2}} \sum_{n=0}^{\infty} \frac{\alpha^n}{\sqrt{n!}} |n\rangle$. It is straightforward to calculate the detection probabilities for both the lowering and subtraction operator back actions, as a function of α:

Lowering Operator

$$P_{\text{low}}(\alpha) \equiv \text{Tr}\left[\hat{a} |\alpha\rangle \langle\alpha| \hat{a}^\dagger\right] = |\alpha|^2 \tag{2.40}$$

Subtraction Operator

$$\begin{aligned} P_{\text{sub}}(\alpha) &\equiv \text{Tr}\left[\hat{B}_{\text{m}} |\alpha\rangle \langle\alpha| \hat{B}_{\text{m}}^\dagger\right] \\ &= 1 - e^{-|\alpha|^2} = |\alpha|^2 - \frac{|\alpha|^4}{2} + O\left(|\alpha|^6\right) \end{aligned} \tag{2.41}$$

As equations (2.40) and (2.41) show, the difference in the detection probabilities occurs only in the nonlinear response, i.e., terms of the order of $|\alpha|^4$. This is consistent with the observation that $\hat{a}$ and $\hat{B}$ have identical matrix elements up to 1 photon but are different at higher photon numbers. By measuring the detection probability for coherent states of varying power and examining how this detection probability scales with the power of the coherent state, it is possible to characterize the back action with respect to the lowering operator and the subtraction operator.

2.6.2 Bare JPM Coherent State Test

First we apply this test to our simulations of a bare JPM, recalling that we expect $\hat{B}^1(t) \sim \hat{a}$ at short times (see equation (2.17)) and $\hat{B}^1(t) \sim \hat{B}_{\mathrm{m}}$ at long times (see discussion in sect. 2.5.1). The proportionality constants affect the detection probability and not the structure of the back action, so we remove them by renormalizing (2.40) and (2.41) as follows:

$$\tilde{P}_{\mathrm{low}}(\alpha) = \frac{P_{\mathrm{low}}(\alpha) P_{\mathrm{data}}(\alpha = \alpha_0)}{P_{\mathrm{low}}(\alpha = \alpha_0)} \tag{2.42}$$

$$\tilde{P}_{\mathrm{sub}}(\alpha) = \frac{P_{\mathrm{sub}}(\alpha) P_{\mathrm{data}}(\alpha = \alpha_0)}{P_{\mathrm{sub}}(\alpha = \alpha_0)} \tag{2.43}$$

where P_{data} is the simulated detection probability, and α_0 is the smallest value of α with simulated data. The α-scaling of the JPM can be more directly compared to those of these rescaled lowering and subtraction operators. Experimentally, this is important as it accounts for calibration uncertainties that may occur, such as from attenuation or imperfect impedance matching.

Figures 2.12(a) and 2.12(d) show the detection probabilities of a bare JPM as a function of the power of the coherent input state α for a gt_m value of 0.126 and 12.6 respectively. As expected, the back action is very close to the lowering operator at short times – only deviating slightly at high powers – and at long times the back action is very close to the subtraction operator. At short times, the deviation from the lowering operator at high powers can be explained by equation (2.17), which only predicts the back action will be proportional to $\hat{a}$ for $\sqrt{n}gt \ll 1$. Thus, at high powers (large $|\alpha| = \sqrt{n}$), corrections to (2.17) will become important, as is this case for measurement times long compared to $t_{\mathrm{crit}} = (g\sqrt{n})^{-1}$. Figures 2.12(b) and 2.12(c) show the back action at intermediate times. While 2.12(b) shows behavior intermediate between the lowering and subtraction operators, figure 2.12(c) shows that α-scaling can actually fall below that of

the subtraction operator. This effect is a result of the additional dephasing incurred in measurement.

2.6.3 The Effects of Pure Dephasing and Energy Relaxation

We now study the affects of energy relaxation and pure dephasing on the α-scaling of the coherent state test. Figure 2.13 shows the detection probability of a JPM experiencing energy relaxation at a rate $\frac{1}{T_1} = \gamma_1$ as a function of α, at the same times as those of figure 2.12. As can be seen in figure 2.13(d) (which represents the long time steady state of the back action), the major effect of energy relaxation is to prevent the back action from fully transitioning to the subtraction operator at long times, but rather it asymptotes to an operator in the intermediate regime. With the additional energy relaxation channel present, the JPM detection probability becomes more sensitive to the number of photons in the cavity and does not fully approach the subtraction operator, which cannot resolve photon number.

In addition, energy relaxation suppresses the sub-subtraction scaling at intermediate times (see figure 2.13(c)). We expect this is due to the added dephasing at $T_2 = 2T_1$, since figure 2.14 shows that dephasing alone suppresses the drop below that of the subtraction operator at intermediate times (figure 2.14(c)). As can be seen, the effect of pure dephasing on α-scaling is similar to that of energy relaxation; however, instead of stopping the back action from transitioning to the subtraction operator, pure dephasing merely increases the time scale on which this transition occurs.

2.7 Optimal Regime for a JPM

Albeit based on a similar circuit, the bare operation conditions for the JPM are different from those of a phase qubit, where long T_1 and T_2 are highly

desirable. Operating a JPM at extremely long T_2 leads to the phenomenon of oscillating detection probability (figure 2.2), sub-subtraction back action (figure 2.12(c)) and additional dephasing of the cavity (figure 2.2(b)). This additional dephasing is undesirable as it destroys coherences in the original cavity state, irreversibly reducing its off-diagonal matrix elements, hence limiting the information available in a repeated measurement.

It is thus advisable to operate the JPM in the short T_2 regime. However, the effective photon-detector transfer rate, eq. (2.36), should be much shorter than the decoherence rate of the cavity, and this places a lower bound on T_2. On the other hand, T_1-processes always limit the measurement fidelity and should be avoided. One way to achieve the limit of long T_1 with short T_2 is to damp the JPM with a frequency-dependent impedance with lowpass character, e.g., along the lines of [75], by shunting the JPM with an LR-element.

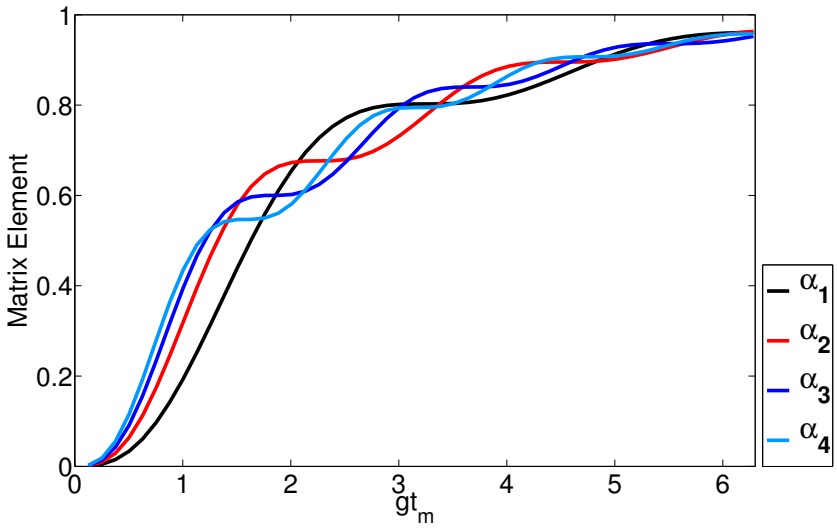

(a) Bare JPM Diagonal Matrix Elements

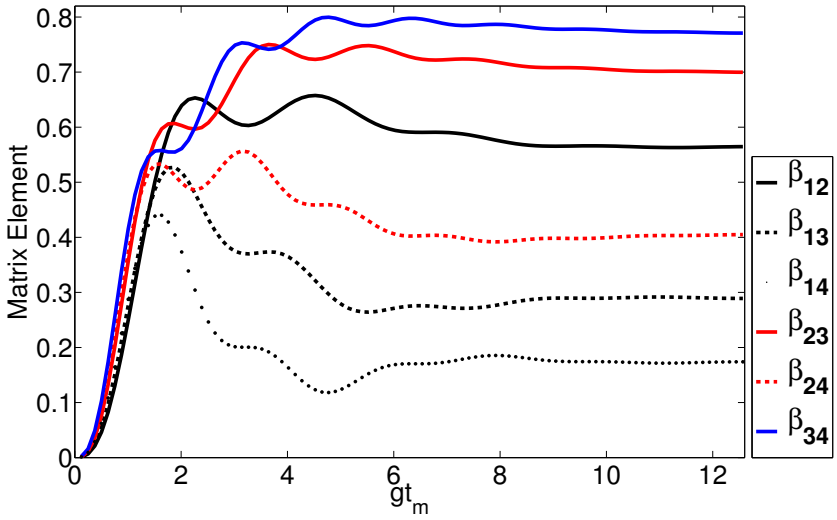

(b) Bare JPM Off-Diagonal Matrix Elements

Figure 2.2: (a) Diagonal and (b) off-diagonal χ^1-matrix elements for a bare JPM as a function of time, where $\alpha_j = \beta_{jj}$ as defined in equation 2.20.

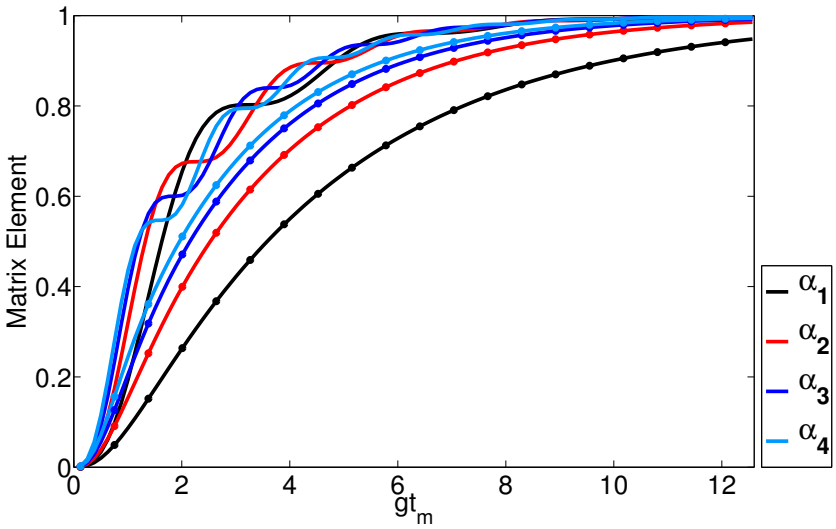

(a) Bare JPM and Pure Dephasing Diagonal Matrix Elements

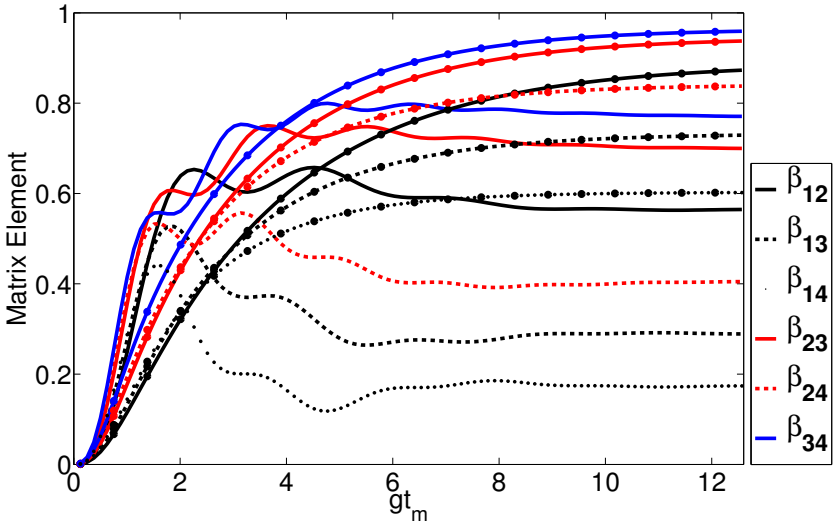

(b) Bare JPM and Pure Dephasing Off-Diagonal Matrix Elements

Figure 2.3: Comparison of the (a) diagonal and (b) off-diagonal χ^1-matrix elements of a bare JPM with one experiencing additional pure dephasing $1/T_2 = 10\gamma_1$ (marked with circles). In both plots, each curve's color indicates its row in the χ^1-matrix, and in (b), distance from the diagonal is indicated by line style.

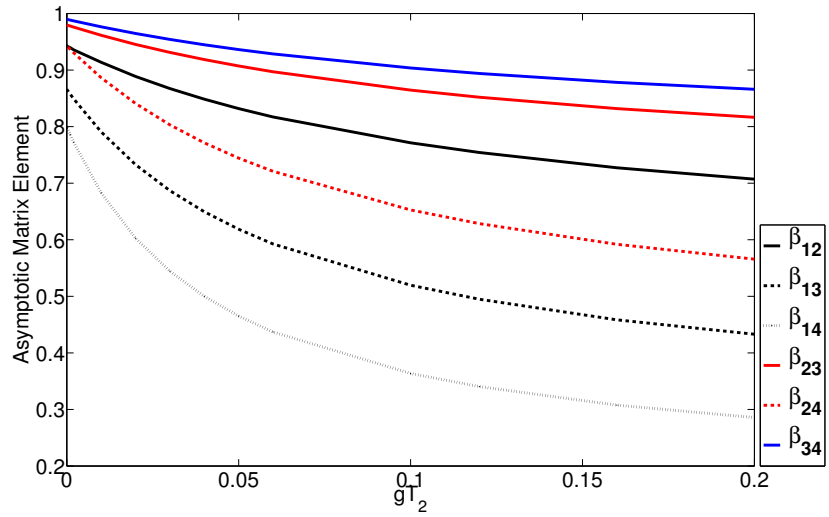

(a) Off-Diagonal Asymptotic Limits

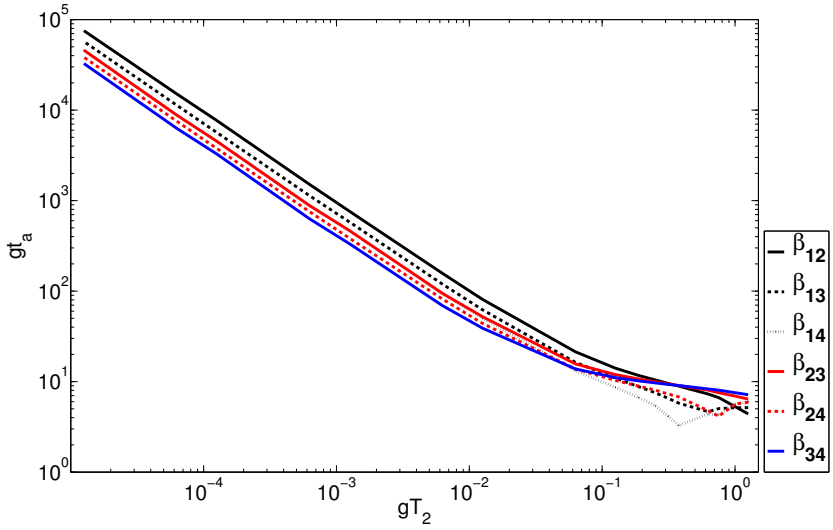

(b) Off-Diagonal Asymptotic Time Scale

Figure 2.4: Figure (a) shows the asymptotic limit of the off-diagonal χ^1 matrix elements as a function of T_2, and figure (b) shows the timescale over which these asymptotic limits are reached. Figure (b) is not monotonic due to the coherent oscillations present for long T_2.

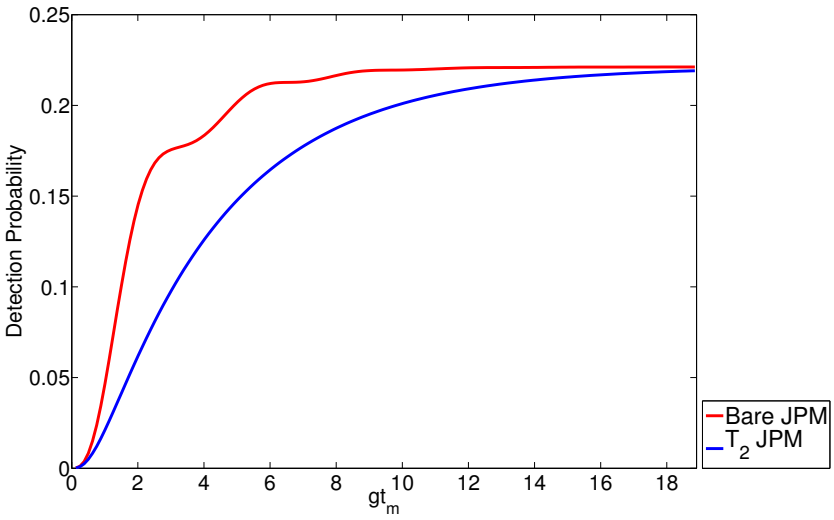

(a) Coherent State Detection Probability

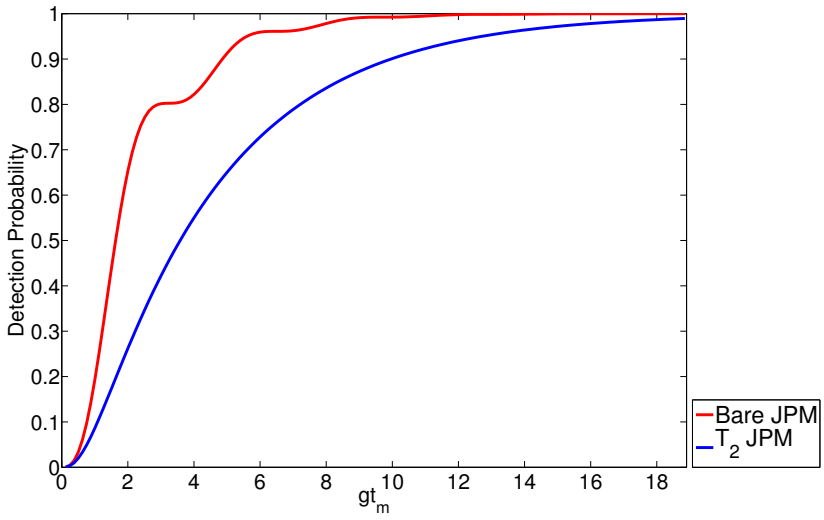

(b) One Photon Fock State Detection Probability

Figure 2.5: Figure (a) shows the detection probability for a bare JPM and a JPM experiencing pure dephasing for a coherent state input (as described in section (2.6.1) with $|\alpha| = 0.5$). Figure (b) shows the detection probability for a bare JPM and a JPM experiencing pure dephasing for a one photon Fock state input.

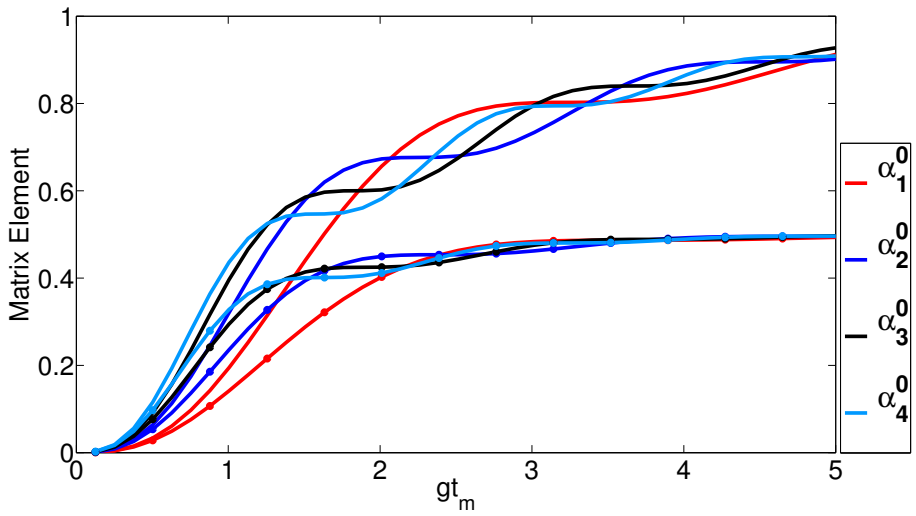

Figure 2.6: This figure shows the diagonal χ^1 matrix elements shared by a bare JPM and a JPM experiencing energy relaxation. Energy relaxation matrix elements are represented by cirlces on the plots.

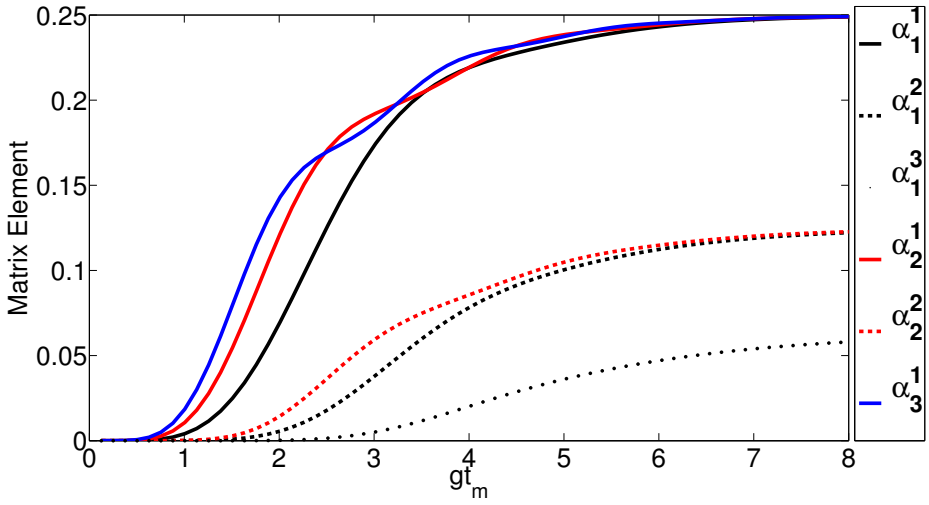

Figure 2.7: Diagonal χ^1-matrix elements $\alpha_j^{(r)} \equiv \chi^1_{j-1j+rj-1j+r}$ corresponding to photon detection after loss of r photons. These elements are zero unless an energy dissipation mechanism is present.

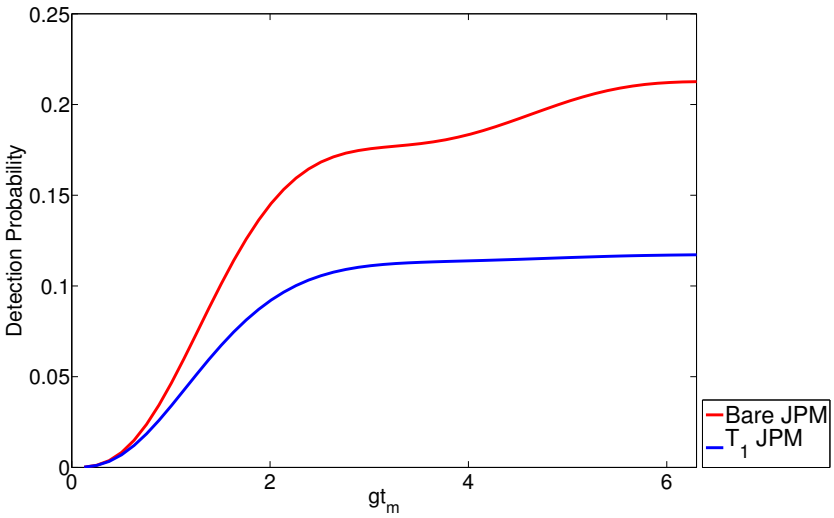

(a) Coherent State Detection Probability

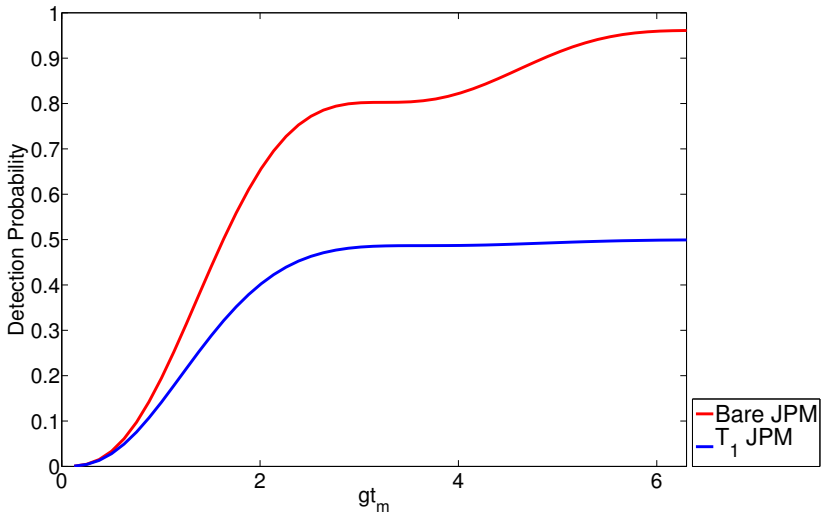

(b) One Photon Fock State Detection Probability

Figure 2.8: Figure (a) shows the detection probability for a bare JPM and a JPM experiencing energy relaxation for a coherent state input (same as in 2.5(a)). Figure (b) shows the detection probability for a bare JPM and a JPM experiencing energy relaxation for a one photon Fock state input (same as in 2.5(b)).

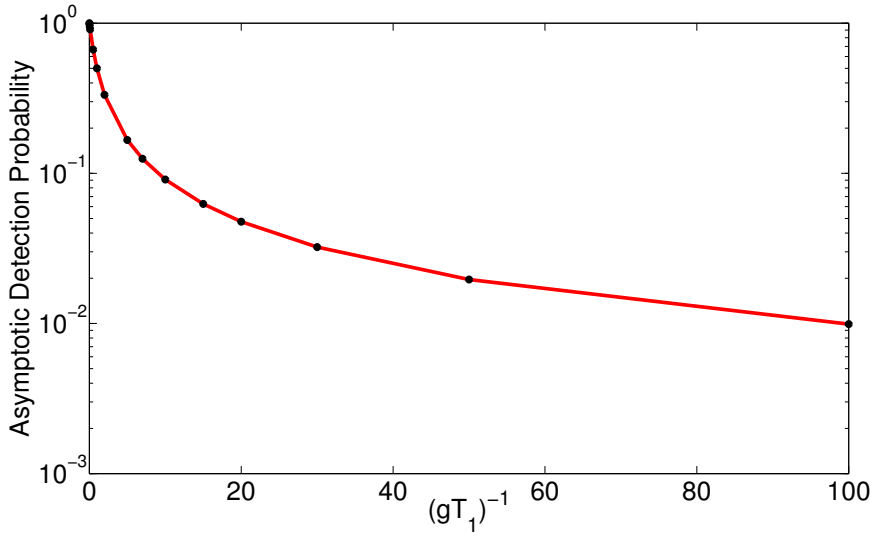

Figure 2.9: This figure shows the asymptotic value of detection probability for a JPM experiencing energy relaxation as a function of the energy relaxation rate T_1^{-1}. The black circles represent numerically simulated data points, while the red curve is a linear fit between the simulated data points. As expected, it is a monotonically decreasing function.

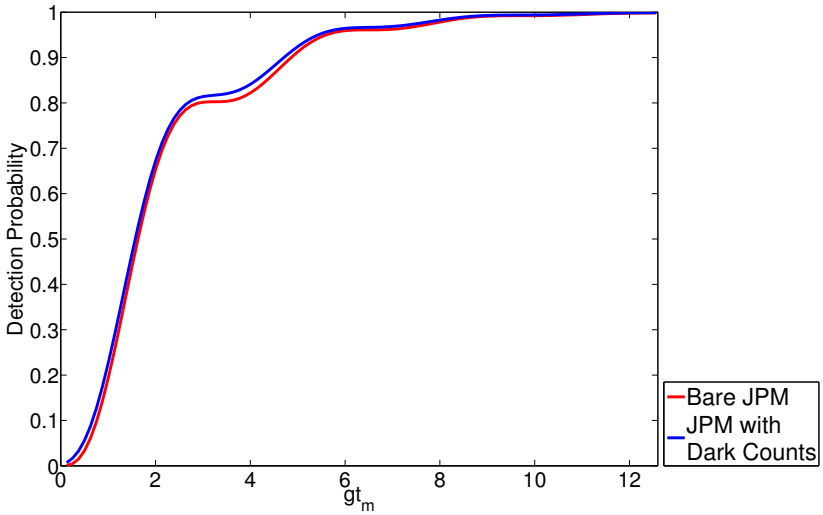

(a) One Photon Fock State Detection Probability

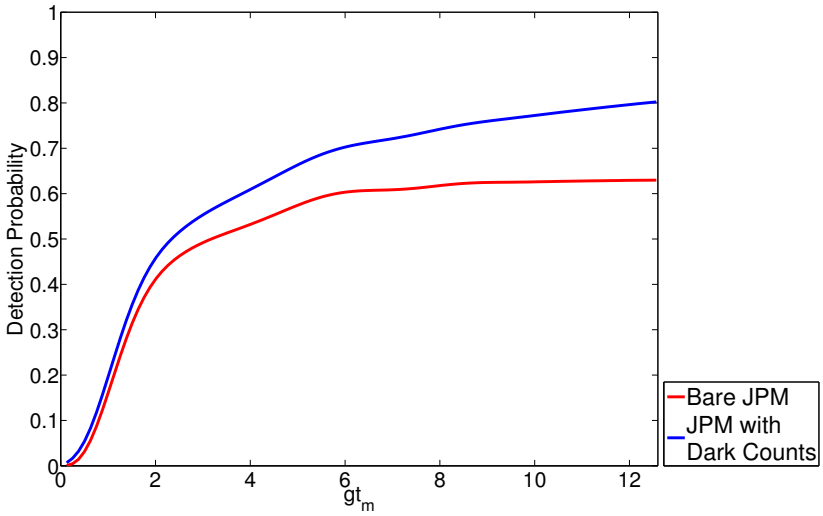

(b) Coherent State Detection Probability

Figure 2.10: Detection probabilities for a bare JPM and one experiencing dark counts for (a) a one-photon Fock state input state and (b) an $\alpha = 1$ coherent state input state.

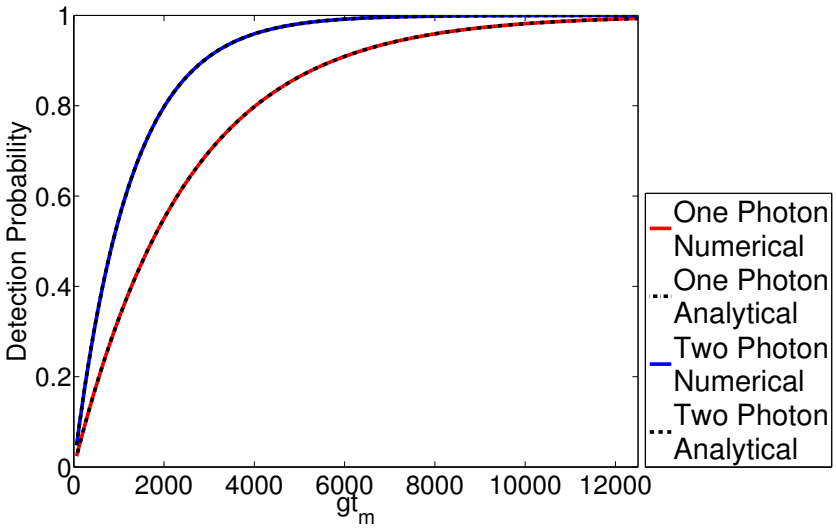

(a) Low T_2 Regime

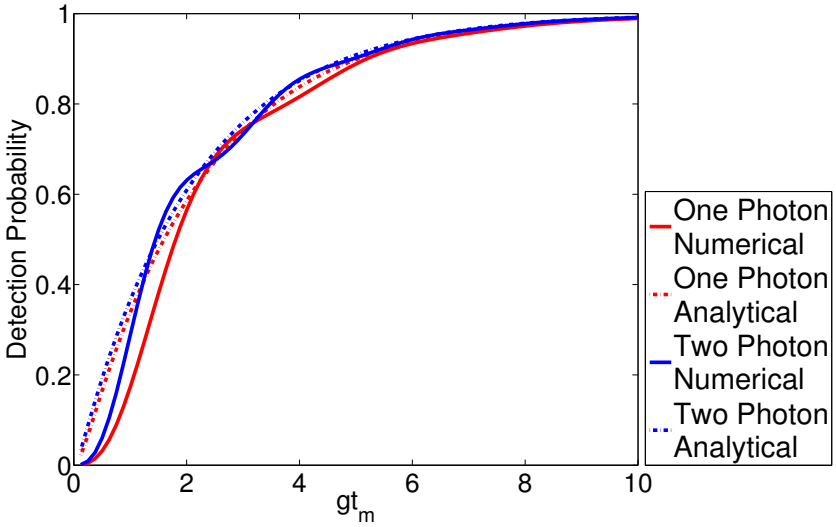

(b) Intermediate T_2 Regime

Figure 2.11: These figures show the detection probability of a JPM experiencing pure dephasing in the low and intermediate T_2 regimes for one and two photon Fock state inputs. The detection probability obtained from the analytical solution described in this section is compared to a numerical simulation (via the Liouville supermatrix approach) of the detection probability. In figure (a) $\frac{1}{T_2} = 10000\gamma_1$ and in figure (b) $\frac{1}{T_2} = \gamma_1$.

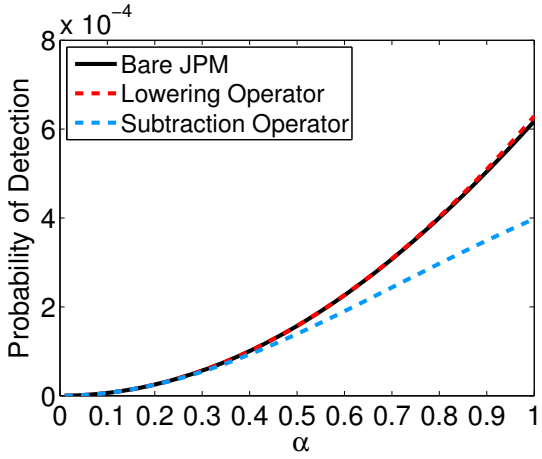

(a) $gt_m = 0.126$ Detection Probability

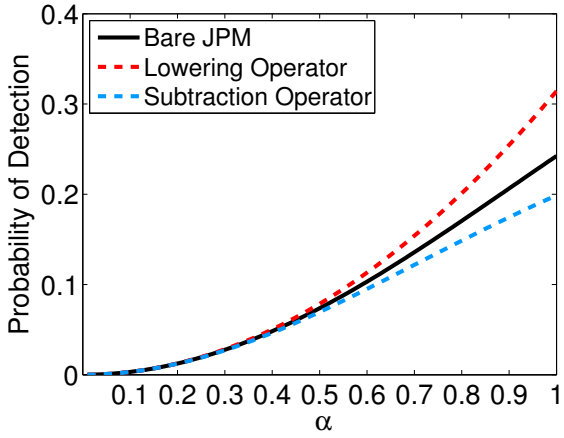

(b) $gt_m = 1.26$ Detection Probability

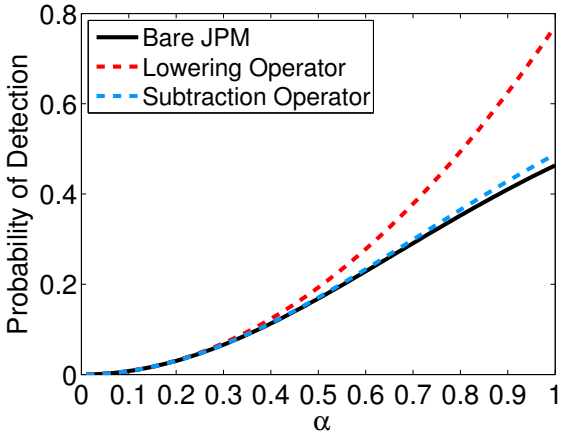

(c) $gt_m = 2.52$ Detection Probability

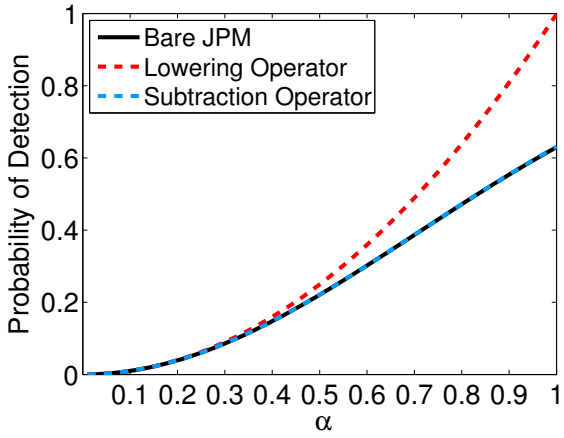

(d) $gt_m = 12.6$ Detection Probability

Figure 2.12: For a bare JPM, the detection probability is shown for a measurement occurring at $t_m g$ values of 0.126 in (a), 1.26 in (b), 2.52 in (c) and 12.6 in (d). α runs from $\alpha = 0.01$ to $\alpha = 1$ in 0.01 intervals, and in each figure, all three curves are scaled to be equal at $\alpha = 0.01$. The time in (d) is chosen such that it is representative of the long time steady state of the back action.

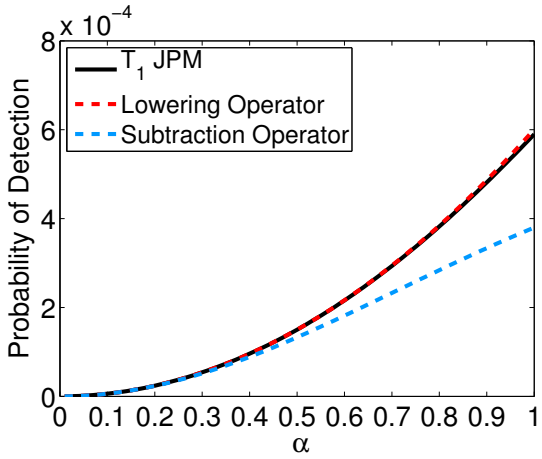

(a) $gt_m = 0.126$ Detection Probability

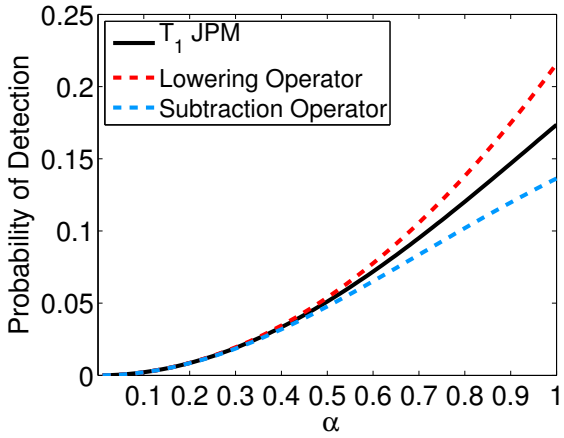

(b) $gt_m = 1.26$ Detection Probability

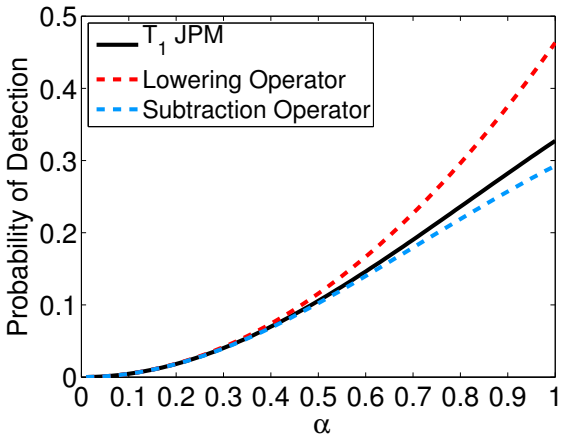

(c) $gt_m = 2.52$ Detection Probability

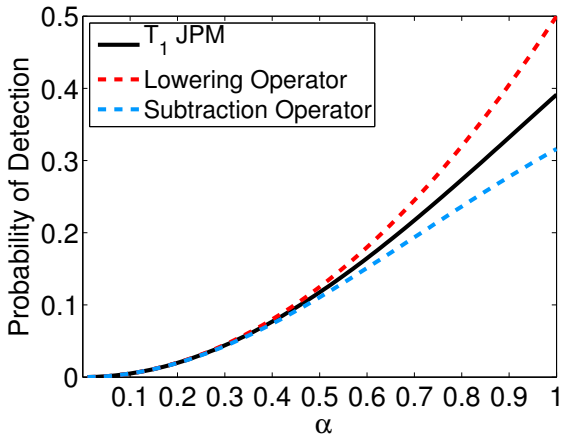

(d) $gt_m = 12.6$ Detection Probability

Figure 2.13: For a JPM experiencing energy relaxation (with $T_1 = \frac{1}{\gamma_1}$ as before), the detection probability is shown for a measurement occurring at $t_m g$ values of 0.126 in (a), 1.26 in (b), 2.52 in (c) and 12.6 in (d). α runs from $\alpha = 0.01$ to $\alpha = 1$ in 0.01 intervals, and in each figure, all three curves are scaled to be equal at $\alpha = 0.01$.

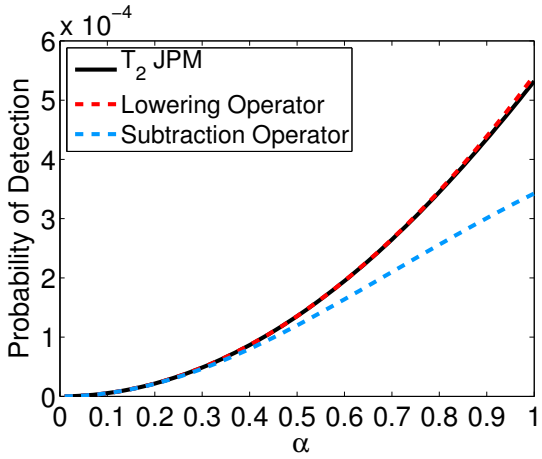

(a) $gt_m = 0.126$ Detection Probability

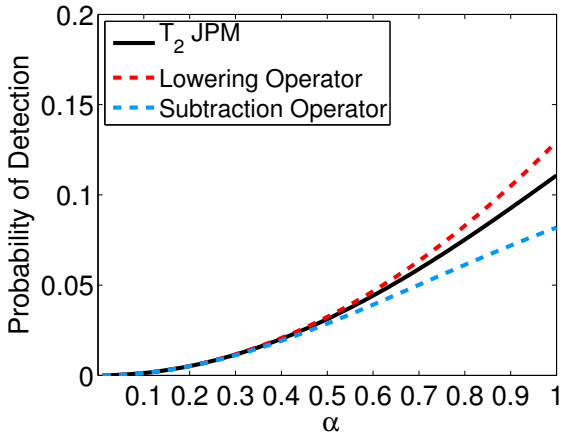

(b) $gt_m = 1.26$ Detection Probability

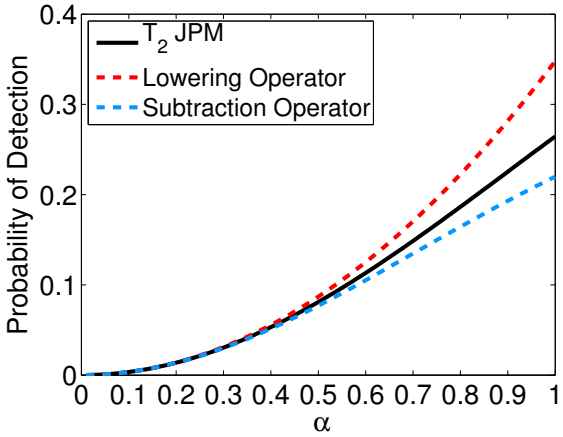

(c) $gt_m = 2.52$ Detection Probability

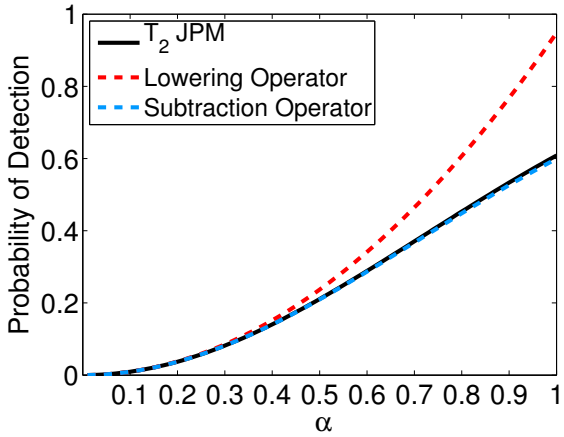

(d) $gt_m = 12.6$ Detection Probability

Figure 2.14: For a JPM experiencing pure dephasing (with $T_2 = \frac{10}{\gamma_1}$ as before), the detection probability is shown for a measurement occurring at $t_m g$ values of 0.126 in (a), 1.26 in (b), 2.52 in (c) and 12.6 in (d). α runs from $\alpha = 0.01$ to $\alpha = 1$ in 0.01 intervals, and in each figure, all three curves are scaled to be equal at $\alpha = 0.01$.

Chapter 3

Non-Classical Light

3.1 Introduction

The generation of non-classical states of light is an important test of the foundations of quantum mechanics and a necessary precursor to implementing quantum communication and computation protocols in many architectures. While the methodology for creating nonclassical light at optical wavelengths has been studied extensively [63, 76, 77], the technology to create quantum states with larger and larger wavelengths has recently become available with advances in circuit-QED.

In the microwave regime, the generation of squeezed states of microwave radiation has been achieved through the use of a Josephson parametric amplifier [54, 78], and the creation of arbitrary non-classical states via the controlled interaction of a superconducting qubit with a microwave cavity has also been achieved [69, 29].

In this chapter we present a novel way to generate non-classical states of microwave radiation in a long wavelength transmission line using only a Josephson Photomultiplier (JPM). Our protocol only involves radiating a microwave cavity with coherent light, and post selection based on single

photon detection by JPMs, on which no direct manipulation is required (except for possible reset). In addition, our protocol applies to any detection mechanism with a back action resembling that of the subtraction operator (equation (3.1)) and so can be generalized to systems other than superconducting circuits [79, 80].

The JPM, a current biased Josephson junction (phase qubit), has been shown experimentally [45] and theoretically [81] to be an effective single photon detector that operates in the microwave regime. Previously, we have shown that for a JPM under optimal conditions the back action of photon detection is the photon subtraction operator [81]:

$$\hat{B} \equiv \sum_{n=1}^{\infty} |n-1\rangle\langle n|. \tag{3.1}$$

a non-linear operator that can be related to the photon lowering operator by $\hat{a} = \hat{B}\sqrt{\hat{n}}$.

In this chapter we show how to use the noncommuntativity of the detection back action and coherent displacement pulses to achieve single mode quadrature squeezing of an input coherent state, and to generate other non-classical states, including the squeezed odd Schrödinger cat state [63] (see chapter 1.4 for more information about non-classical light). We also discuss the success probability of our protocol under realistic operating conditions.

3.2 Squeezed States of Microwave Radiation

The generation of squeezed states of microwave radiation using JPMs follows a simple protocol. The cavity is initially prepared in a coherent state, $|\alpha\rangle = e^{-\frac{|\alpha|^2}{2}} \sum_{n=0}^{\infty} \frac{\alpha^n}{\sqrt{n!}}|n\rangle$ where $\alpha \equiv |\alpha|e^{i\varphi_\alpha}$, and is coupled to one or more JPMs operating in the photon subtraction regime. After N photon detections are

observed (the optimal choice of N will be discussed shortly) a displacement pulse is applied, such that the state is shifted to be centred around the phase space point $-\alpha$. After N further photon detections are observed, the resulting state is a squeezed state.

Starting from the coherent state input, the probability of the coupled JPMs to detect N photons is

$$P_N \equiv 1 - e^{-|\alpha|^2} \sum_{n=0}^{N-1} \frac{|\alpha|^{2n}}{n!} = 1 - \frac{\Gamma(N, |\alpha|^2)}{\Gamma(N)} \tag{3.2}$$

where $\Gamma(N, |\alpha|^2)$ is the upper incomplete gamma function of N and $|\alpha|^2$ [82]. $P_N \sim |\alpha|^{2N}/N!$ as $|\alpha| \to 0$; however, P_N can be made arbitrarily close to unity with larger power coherent state inputs.

It is straightforward to calculate the normalized post measurement cavity state after N detections,

$$\rho' \equiv \frac{\hat{B}^N |\alpha\rangle\langle\alpha| \hat{B}^{\dagger N}}{P_N}, \tag{3.3}$$

and the average photon number $n' \equiv \langle a^\dagger a \rangle_{\rho'}$ is given by

$$n' = \frac{|\alpha|^2 \left(1 - \frac{\Gamma(N-1,|\alpha|^2)}{\Gamma(N-1)}\right) - N \left(1 - \frac{\Gamma(N,|\alpha|^2)}{\Gamma(N)}\right)}{P_N}. \tag{3.4}$$

After N detections, the next step is to displace the state by an amount $\alpha' = -\sqrt{n'} e^{i\varphi_\alpha} - \alpha$, so that the resulting state will be centred in phase space around $-\alpha$. For this displaced state, N photon detection events will occur with probability P'_N (for which the analytic expression is cumbersome and uninstructive), and the renormalized cavity state will have the form

$$\rho'' \equiv \frac{\hat{B}^N D(\alpha') \rho' D(\alpha')^\dagger \hat{B}^{\dagger N}}{P'_N}. \tag{3.5}$$

The state ρ'' is a squeezed state.

To quantify the amount of squeezing, we calculate the variance of the squeezed quadrature

$$\Delta p^2 = \mathrm{Tr}[\rho''\hat{p}^2] - \mathrm{Tr}[\rho''\hat{p}]^2. \tag{3.6}$$

The quadrature observable $\hat{p}$ is defined by $\hat{p} = \frac{1}{\sqrt{2}}\left(\hat{a}e^{-i\varphi_\alpha} - \hat{a}^\dagger e^{i\varphi_\alpha}\right)$, where $\hat{a}$ is the annihilation operator for the cavity microwave mode. The phase shift $e^{-i\varphi_\alpha}$ is necessary to account for the fact that this protocol squeezes along the phase space axes defined by the phase of the input coherent state. Anything less than $\Delta p^2 = \frac{1}{2}$ indicates a squeezed state. The amount of squeezing is most commonly expressed in dB, by calculating

$$S(\Delta p) \equiv 10\log_{10}\left(\frac{\Delta p^2}{\Delta p^2_{\mathrm{norm}}}\right) = 10\log_{10}\left(2\Delta p^2\right). \tag{3.7}$$

In addition, we can calculate how far the state ρ'' deviates form a minimal uncertainty state by calculating $\Delta x \Delta p$ (where $\hat{x} = \frac{1}{\sqrt{2}}\left(\hat{a}e^{-i\varphi_\alpha} + \hat{a}^\dagger e^{i\varphi_\alpha}\right)$ is the conjugate observable to $\hat{p}$). Figures 3.1(a) and 3.1(b) show $S(\Delta p)$ and $\Delta x \Delta p$ respectively as functions of α and the number of detection events on either side of the displacement, N.

As can be see in figure 3.1(a), the maximum amount of squeezing possible on a given input state $|\alpha\rangle$ increases monotonically with $|\alpha|^2$, proportional to the power of the input pulse. Interestingly, for a given α there exists a finite N that achieves a global minimum in Δp^2. One would be tempted to use this value of N in the protocol to create ρ'', however, as can be seen in figure 3.1(b) there are other concerns.

As figure 3.1(b) shows, for a given α, $\Delta x \Delta p$ is not monotonic in N. Since we want ρ'' to be as close to a minimal uncertainty state as possible, while still maintaining a significantly squeezed quadrature, the optimal choice of N for the protocol would be at the $\Delta x \Delta p$ local minima shown in figures

3.1(a) and 3.1(b) by the white curve. While this does not minimize Δp^2 (and therefore maximize squeezing), it achieves a significantly squeezed state ρ'' that is as close to being a minimal uncertainty state as is possible, which is what we consider optimal.

3.3 Generalized Protocol

Non-classical states of microwave radiation, other than the squeezed states described previously, can be created by a generalization to the protocol used to create squeezed states. The squeezed state protocol involves shifts only along one axis in phase space, while in the generalized protocol, the state will be shifted around a circle in phase space, with N detection events occurring at k points on this circle. The squeezed state protocol is the $k = 2$ case of the generalized protocol.

There are k steps to the generalized protocol, with each step following the same pattern. As before, we begin with a coherent input state $\rho_0 = |\alpha\rangle \langle\alpha|$. Each step of the generalized protocol consists of two stages: the detection stage, where N detection events occur, and the displacement stage, where a driving pulse is applied to displace the state to the next point in the protocol. After the detection stage of the j'th step, the system will be in the state

$$\tilde{\rho}_j \equiv \frac{\hat{B}^N \rho_{j-1} \hat{B}^{\dagger N}}{P_N^{j-1}}, \tag{3.8}$$

where P_N^{j-1} is the probability of N photon detections occurring for the state ρ_{j-1}. This state has average photon number $n_j = \left\langle a^\dagger a \right\rangle_{\tilde{\rho}_j}$. The displacement stage of the j'th step consists of applying a coherent pulse with amplitude

$$\alpha_j = -\sqrt{n_j} e^{i(\varphi_\alpha + (j-1)\varphi_k)} + |\alpha| e^{i(\varphi_\alpha + j\varphi_k)}, \tag{3.9}$$

where $\varphi_k = \frac{2\pi}{k}$. This results in the new state

$$\rho_j = \frac{D(\alpha_j)\hat{B}^N \rho_{j-1} \hat{B}^{\dagger N} D(\alpha_j)^\dagger}{P_N^{j-1}}. \tag{3.10}$$

The desired non-classical state will be created when ρ_k is reached.

At the end of the generalized protocol, the output state ρ_k will have average photon number $n'_k = \left\langle a^\dagger a \right\rangle_{\rho_k}$. If we displace by a coherent pulse with $\alpha'_k = -\sqrt{n'_k} e^{i\varphi_\alpha}$, the resulting state will be centred at the origin of phase space. This is done to simplify comparison to known analytic states.

As mentioned previously, the case $k = 2$ ($\varphi_k = \pi$) corresponds to the creation of a state with squeezed quadratures. This state is in fact very close to a squeezed vacuum state

$$|\Psi_2\rangle = S(z)\,|0\rangle = e^{-\frac{1}{2}\left(z(\hat{a}^\dagger)^2 - z^*(\hat{a})^2\right)}\,|0\rangle \tag{3.11}$$

where $S(z)$ is the squeezing operator with complex squeezing parameter z, which has to be found numerically.

In general, for $k \geq 2$ the states created by the generalized protocol are very close to the analytic states

$$|\Psi_k\rangle = S^{(k)}(z)\,|0\rangle = e^{-\frac{1}{2}\left(z(\hat{a}^\dagger)^k - z^*(\hat{a})^k\right)}\,|0\rangle\,, \tag{3.12}$$

where $S^{(k)}(z)$ is what we call a generalized displacement-squeezing class operator with complex parameter z (which has to be found numerically). The first three operators of this class are shown below

$$S^{(0)}(z) = e^{-\frac{1}{2}\mathrm{Im}[z]\mathbb{I}} \tag{3.13}$$

$$S^{(1)}(z) = D\left(-\frac{z}{2}\right) \tag{3.14}$$

$$S^{(2)}(z) = S(z) \tag{3.15}$$

where $S(z)$ is the squeezing operator of equation (3.11).

To find z, we impose the condition that $D(\alpha'_k)\rho_k D(\alpha'_k)^\dagger$ and $|\Psi_k\rangle$ have the same average photon number by setting

$$\left\langle D(\alpha'_k)^\dagger a^\dagger a D(\alpha'_k)\right\rangle_{\rho_2} = \langle\Psi_k| a^\dagger a |\Psi_k\rangle . \tag{3.16}$$

This results in excellent fidelity between the states, quantified by

$$\mathrm{F}\left[\rho_k\right] \equiv \mathrm{Tr}\left[D(\alpha'_k)\rho_k D(\alpha'_k)^\dagger |\Psi_k\rangle \langle\Psi_k|\right] . \tag{3.17}$$

In fact, for $k = 2$ and $|\alpha| = 3$ the fidelity is $> 99\%$.

To verify that these states are indeed non-classical, a suitable non-classicality witness can be used. For this purpose, we use the entanglement potential of [83], defined by

$$\mathrm{EP}[\rho] \equiv \log_2 ||\sigma_\rho^{T_A}||_1, \tag{3.18}$$

where $\sigma_\rho = U_{\mathrm{BS}}\left(\rho \otimes |0\rangle\langle 0|\right) U_{\mathrm{BS}}^\dagger$, for U_{BS} the unitary transformation of a 50:50 beam splitter, and $\sigma_\rho^{T_A}$ is the partial transpose of σ_ρ [84]. A nonzero entanglement potential indicates that the state ρ is non-classical, and indeed, as can be calculated numerically, the states created by the generalized protocol all have nonzero entanglement potential. The entanglement potential of these states is plotted in figure 3.2 as a function of the number of detections at each step of the protocol.

The success probability for the generalized protocol can be calculated by the product

$$\mathrm{Prob(success)} = \prod_{j=0}^{k-1} P_N^j. \tag{3.19}$$

Since the displacement stage of each step ensures the average photon number of each state ρ_j is on the order of $|\alpha|^2$, each P_N^j can be quite large, and as a result, the generalized protocol will have a significant probability of success. For example, for a modest $|\alpha| = 3$ the success probability for $k = 2, 3$ or 4 is $\approx 85\%$. Furthermore, the success probability will scale monotonically with $|\alpha|$, and so can be increased by increasing the initial input state power.

The generalized protocol previously described can also be simply extended to create additional non-classical states, including the squeezed odd Schrödinger cat state, with only a single additional detection required. Starting from the output state displaced to the origin $D(\alpha'_k)\rho_k D(\alpha'_k)^\dagger$, after a single detection event has occurred, the resulting state has the form

$$\rho'_k = \frac{\hat{B}D(\alpha'_k)\rho_k D(\alpha'_k)^\dagger \hat{B}^\dagger}{P_1^k}, \tag{3.20}$$

where P_1^k is the probability of a single photon detection occurring for the state $D(\alpha'_k)\rho_k D(\alpha'_k)^\dagger$.

For $k = 2$, this additional detection will create a state very close to a squeezed odd Schrödinger cat state

$$|\Psi'_2\rangle \equiv S^{(2)}(z)\left(|\beta\rangle - |-\beta\rangle\right), \tag{3.21}$$

where now both z and β have to be found numerically (via a similar procedure as before). The Husimi Q function of the state ρ'_2 (input $|\alpha| = 3$) is shown in figure 3.3. As can be seen, it has similar structure to the odd Schrödinger cat state shown in figure 1.3, with the differences a result of the fact that the state ρ'_2 is squeezed.

The probability of successful generation of these additional non-classical states is

$$\text{Prob(success)}' = P_1^k \prod_{j=0}^{k-1} P_N^j. \tag{3.22}$$

Unfortunately, due to the fact that it is centred at the origin, $D(\alpha'_k)\rho_k D(\alpha'_k)^\dagger$ will have a very low average photon number. As a result, it is often the case that $P_1^k \ll 1$, which results in a limited probability of success. For example, for $k = 2$ and $|\alpha| = 3$, the probability of successful generation of a squeezed odd Schrödinger cat state is $\approx 10\%$. However, the monotonic scaling with $|\alpha|$ is unaffected, so this problem can be somewhat mitigated by increasing the input state power.

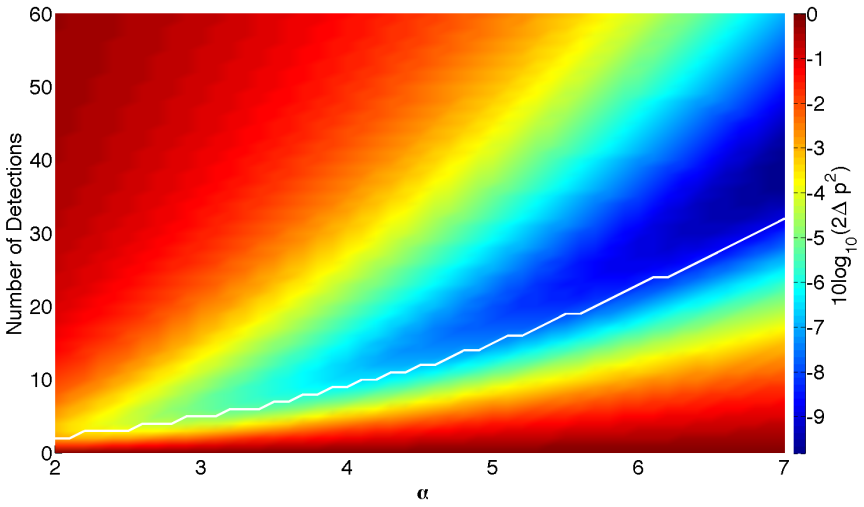

(a)

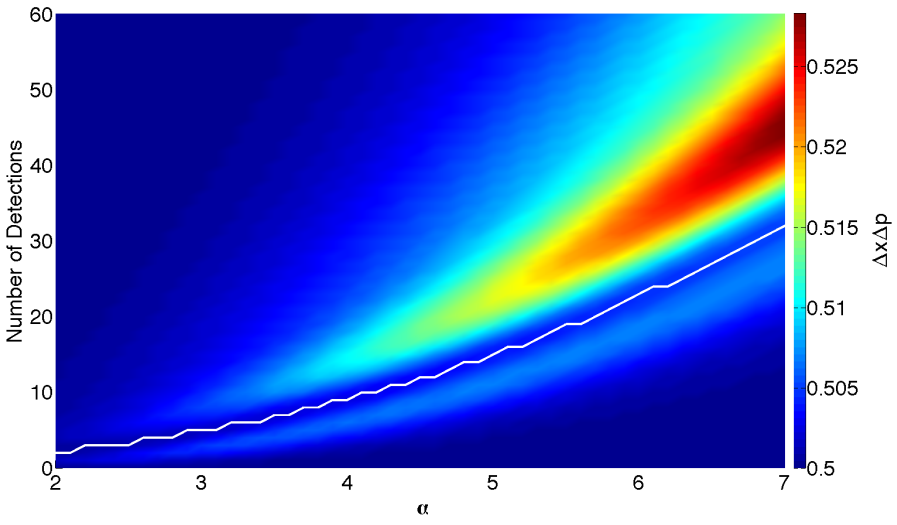

(b)

Figure 3.1: (a) $S(\Delta p)$ and (b) $\Delta x \Delta p$ of the state ρ'', as functions of α and the number of detection events, N. $\varphi_\alpha = 0$ for both figures. The white curve indicates the value of N that gives a local minimum in $\Delta x \Delta p$, while maintaining a squeezed Δp^2.

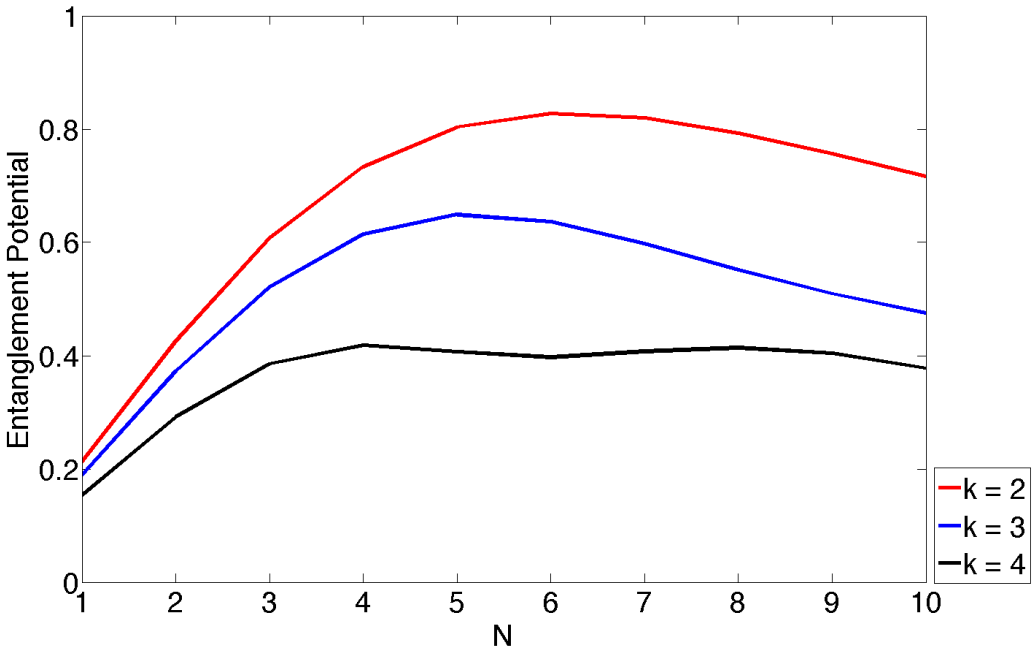

Figure 3.2: This figure shows entanglement potential (EP) of the states created by the generalized protocol (for $k = 2, 3, 4$) as a function of the number of detections, N, performed at each step in the protocol.

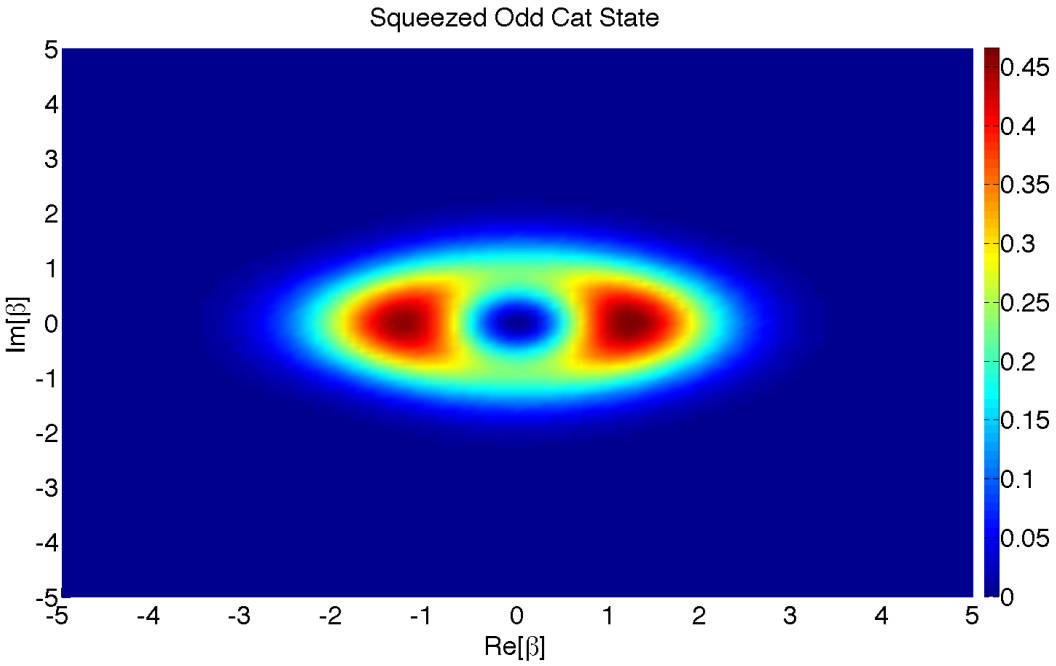

Figure 3.3: This figure shows the Husimi Q function for the state ρ_2' for $|\alpha| = 3$. The double peaked structure of the distribution, corresponding to the two coherent state components centred at α and $-\alpha$, is clearly evident.

Chapter 4

Conclusion

This thesis consists of two main parts. In Chapter 2 we have analyzed the back action of a JPM on the microwave cavity state it measures. Numerical investigations of the cavity χ matrix conditioned on a detection event give us a convenient quantitative description of the detection process while including several relevant environmental processes. At short times, the back action of a bare JPM is similar to the lowering operator, while at long times, the back action approaches the subtraction operator with additional cavity dephasing. This additional dephasing can be reduced by adding pure dephasing to the JPM, which dampens the coherent oscillations between the JPM and the cavity without compromising the purity of the cavity state. Energy relaxation decreases the asymptotic value of the diagonal cavity χ matrix elements and the detection probability by a factor of $\gamma_1/(\gamma_1 + T_1^{-1})$. It is useful to develop a test to determine which regime the JPM is operating in for different measurement times, and the coherent state test is one such test that is straightforward to implement.

In Chapter 3 we have shown how the non-linearity of the JPM back action in the subtraction operator regime can be used to generate non-classical states of microwave radiation. The non-classicality of these states was confirmed by calculating their entanglement potential, and examples

of the states created include the squeezed vacuum state, and the squeezed odd Schrödinger Cat state. The general protocol for generation of these non-classical states has in many cases both a high probability of success, and a high fidelity with the ideal analytic state.

APPENDICES

Appendix A

Mathematical Methods to Simulate the Master Equation

A.1 Quantum Trajectories

A quantum trajectory can be understood as the evolution of a state vector, $|\psi\rangle$, that is subject to both coherent (Hamiltonian dynamics) and incoherent (such as measurement or spontaneous decay) processes. For each incoherent process (described by a Lindblad operator $\hat{\mathcal{J}}_\mu$), we define $N_\mu(t)$ as the number of "jumps" (measurements, decays, etc.) that have occurred up to time t. It is then possible to define a set of stochastic increments $\{dN_\mu(t)\}_\mu$, which satisfy the following properties

$$\mathrm{E}[dN_\mu(t)] = \langle\psi(t)|\,\hat{\mathcal{J}}_\mu^\dagger\hat{\mathcal{J}}_\mu\,|\psi(t)\rangle\,dt \tag{A.1}$$

$$dN_\mu(t)dN_\nu(t) = dN_\mu(t)\delta_{\mu\nu} \tag{A.2}$$

where $\mathrm{E}[a(t)]$ is the expected value of the stochastic increment $a(t)$. Equation (A.2) implies that $dN_\mu(t) = 0$ or $1\ \forall\ \mu$, as is expected, since for a given infinitesimal increment of time dt, at most one "jump" can occur for each incoherent process.

Using the stochastic increments defined above, we can derive the stochastic Schrödinger equation (SSE), which completely describes the evolution of the state vector under both coherent and incoherent dynamics.

$$d\left|\psi(t)\right\rangle = \tag{A.3}$$
$$\sum_{\mu}\left[dN_{\mu}(t)\left(\frac{\hat{\mathcal{J}}_{\mu}}{\sqrt{\left\langle\hat{\mathcal{J}}_{\mu}^{\dagger}\hat{\mathcal{J}}_{\mu}\right\rangle(t)}}-\hat{\mathbb{I}}\right)+dt\left(\frac{\left\langle\hat{\mathcal{J}}_{\mu}^{\dagger}\hat{\mathcal{J}}_{\mu}\right\rangle(t)-\hat{\mathcal{J}}_{\mu}^{\dagger}\hat{\mathcal{J}}_{\mu}}{2}-i\hat{H}\right)\right]\left|\psi(t)\right\rangle$$

The first term describes the incoherent quantum "jump" when $dN_{\mu}(t)=1$, and the second term describes the coherent evolution. For further information, and an explicit derivation of this equation, see reference [85].

The simplest method to numerically simulate equation (A.3) will know be outlined, following reference [85]. A random number $R\in[0,1]$ is generated, and the state is allowed to evolve under the unnormalized evolution

$$\frac{d}{dt}\left|\tilde{\psi}(t)\right\rangle=-\left(\sum_{\mu}\frac{\hat{\mathcal{J}}_{\mu}^{\dagger}\hat{\mathcal{J}}_{\mu}}{2}+i\hat{H}\right)\left|\tilde{\psi}(t)\right\rangle \tag{A.4}$$

until a time T such that $\left\langle\tilde{\psi}(T)\middle|\,\tilde{\psi}(T)\right\rangle=R$. This time T represents the time the first jump occurs, and because equation (A.4) describes only the coherent evolution, the correct statistics for T are guaranteed.

One of the Lindblad operators $\mathcal{J}_{\mu}$ is then applied to the state $\left|\tilde{\psi}(T)\right\rangle$ and the resulting state renormalized. This procedure is repeated (treating $t=T$ like $t=0$) until the desired total evolution time is reached. Determining which incoherent process occurs is also a random event. The unit interval is broken up into N_{inc} bins, one for each incoherent process. For the μ'th

incoherent process, the size of the bin is determined by

$$\frac{\left\langle \tilde{\psi}(T)\right| \hat{\mathcal{J}}_\mu^\dagger \hat{\mathcal{J}}_\mu \left|\tilde{\psi}(T)\right\rangle \delta t}{P_{\text{jump}}} \tag{A.5}$$

where

$$P_{\text{jump}} = \sum_{\mu}^{N_{\text{inc}}} \left\langle \tilde{\psi}(T)\right| \hat{\mathcal{J}}_\mu^\dagger \hat{\mathcal{J}}_\mu \left|\tilde{\psi}(T)\right\rangle \delta t \tag{A.6}$$

and δt is the numerical time increment used in the simulation. Either R or a different randomly generated number from the unit interval can then be used to determine which incoherent process occurs.

In order to correctly simulate the average dynamics of an initial state $|\psi(0)\rangle$, the protocol described above must be repeated a large number of iterations, N. For N large enough, we can approximate the final state density matrix, $\rho(t_{\text{fin}})$, by an ensemble average of the set of output states from the N iterations of the SSE protocol, $\{|\psi(t_{\text{fin}})\rangle_i\}_{i=1}^N$.

$$\rho(t_{\text{fin}}) \approx \mathrm{E}\left[|\psi(t_{\text{fin}})\rangle \langle\psi(t_{\text{fin}})|\right] \tag{A.7}$$

The advantage of the SSE protocol over direct numerical simulate of the master equation is that the time taken to compute the SSE protocol scales as d^2N, where d is the dimension of Hilbert space, while the time taken to compute a master equation simulation scales as d^4 [85]. Thus, for $N < d^2$, the SSE protocol will be faster.

In addition, the SSE protocol would allow us to determine if uncertainty in the "jump" time results in a dephasing like effect in the final state density matrix. Unfortunately, for the problem of simulating a JPM coupled to a microwave cavity (with photon number in the cavity on the order of 10), it was found that $N \gg d^2$, and thus, the SSE protocol was impractical. As a result, it was abandoned, and replaced by the technique described in the following section.

A.2 Vectorized Master Equation and the Liouville Supermatrix

To numerically solve a master equation of the form (2.2), the first step is to vectorize the equation. There are two common ways to do this, and the convention chosen here is row stacking, an example of which is shown below.

$$A = \begin{pmatrix} a_{11} & a_{12} & a_{13} \\ a_{21} & a_{22} & a_{23} \\ a_{31} & a_{32} & a_{33} \end{pmatrix} \longmapsto \mathrm{vec}(A) \equiv \vec{A} = \begin{pmatrix} a_{11} \\ a_{12} \\ a_{13} \\ a_{21} \\ a_{22} \\ a_{23} \\ a_{31} \\ a_{32} \\ a_{33} \end{pmatrix} \tag{A.8}$$

Using the identity

$$\mathrm{vec}(ABC) = A \otimes C^T \vec{B} \tag{A.9}$$

where C^T is the transpose of C, it is possible to express terms of the form $\hat{J}_\mu \xi(t) \hat{J}_\mu^\dagger$ in vectorized notation, and so obtain the vectorized master equation

$$\dot{\vec{\xi}}(t) = \mathcal{S}\vec{\xi}(t) \tag{A.10}$$

where $\mathcal{S}$ is given by equation (2.8).

For a given input state $\vec{\xi}(0)$, equation (A.10) can be solved for the final state, $\vec{\xi}(t)$, by any numerical method used to solve ordinary differential equations. This solution can then converted to the final state density matrix $\xi(t)$. However, as we are more interested in the back action of the JPM, a property independent of the input state, this was not done. Instead, taking inspiration from process tomography, we calculate the Liouville supermatrix, $\mathcal{T}(t) = e^{\mathcal{S}t}$, which completely describes the back action of the JPM.

This is done using the native numerical matrix exponentiation routine in MATLAB.

The Liouville supermatrix is not a commonly used representation for a quantum process, and so through a simple permutation of components, we transform the Liouville supermatrix into the χ-matrix, as defined by equation (2.9). As explained in section 2.4, as we assume the JPM initially starts in its ground state, and are only interested in the final state of the cavity, the full χ-matrix is unnecessary. It is sufficient to look at the reduced χ-matrix, χ^s, conditioned on whether or not a photon detection event has occurred.

To understand the dynamics of particular input states (as used to obtain the detection probabilities shown in figure 2.5, etc.), we calculate the Kraus operators for the quantum process describing a JPM's interaction with a microwave cavity. This allows us to calculate the final state at any time via the equation

$$\xi(t) = \sum_i \hat{A}_i(t)\xi(0)\hat{A}_i(t)^\dagger \tag{A.11}$$

In order to calculate the Kraus operators we first diagonalize the reduced χ-matrix

$$\chi^s_{ij}(t) = \sum_{mn} U_{im}(t)d^s_m(t)\delta_{mn}\bar{U}_{jn}(t) \tag{A.12}$$

where $U^\dagger(t)$ diagonalizes $\chi^s(t)$ and $d^s(t)$ is the resulting diagonal matrix. We then use the formula [1]

$$\hat{A}_i(t) = \sqrt{d^s_i(t)} \sum_j U_{ji}(t)\hat{E}_j \tag{A.13}$$

to obtain the Kraus operators, where $\hat{E}_{j(n,m)} = |n\rangle \langle m|$ is the standard basis for $\mathcal{L}(\mathcal{H}_c)$ derived from the Fock state basis for $\mathcal{H}_c$.

Appendix B

Low T_2 Analytics

B.1 Approximate Solution to the Full Differential Equations

The four first order operator differential equations of equation (2.27) can be reduced to the following fourth order operator differential equation:

$$
\begin{aligned}
0 = {} & \rho_{11}^{(4)} + (\kappa_2 + 2\gamma_1)\rho_{11}^{(3)} + \left[\left(\frac{\kappa_2 + \gamma_1}{2} \right) \left(\frac{\kappa_2 + 5\gamma_1}{2} \right) + 2\mathcal{D}_0 + 4g^2 \right] \rho_{11}^{(2)} \\
& + \left[(\kappa_2 + 2\gamma_1)(2g^2 + \mathcal{D}_0) + \gamma_1 \left(\frac{\kappa_2 + \gamma_1}{2} \right)^2 \right] \rho_{11}^{(1)} \\
& + \left[4g^2 + \mathcal{D}_0 \circ \mathcal{D}_0 + 2g^2\gamma_1 \left(\frac{\kappa_2 + \gamma_1}{2} \right) + 4g^2\mathcal{D}_0 + \gamma_1 \left(\frac{\kappa_2 + \gamma_1}{2} \right) \mathcal{D}_0 \right] \rho_{11} \\
& - 4g^4 \hat{a}\hat{a}^\dagger \rho_{11} \hat{a}\hat{a}^\dagger
\end{aligned}
\tag{B.1}
$$

The superoperator $\mathcal{D}_0[f] \equiv g^2\{\hat{a}^\dagger\hat{a}, f\} = g^2(\hat{a}^\dagger\hat{a}f + f\hat{a}^\dagger\hat{a})$ is introduced for notational convenience. We restrict ourselves to the occupation probability of the cavity state $|n\rangle \langle n|_c$ (see equation (2.30)) and define $x(t) \equiv$

$\langle n|_c \rho_{11}(t) |n\rangle_c$. Equation (B.1) becomes

$$0 = x^{(4)} + (\kappa_2 + 2\gamma_1)x^{(3)} + \left[\left(\frac{\kappa_2 + \gamma_1}{2} \right) \left(\frac{\kappa_2 + 5\gamma_1}{2} \right) + 4g^2 n + 4g^2 \right] x^{(2)}$$
$$+ \left[(\kappa_2 + 2\gamma_1)(2g^2 + 2g^2 n) + \gamma_1 \left(\frac{\kappa_2 + \gamma_1}{2} \right)^2 \right] x^{(1)} + \Bigg[4g^2 + 4g^4 n^2$$
$$+ 2g^2 \gamma_1 \left(\frac{\kappa_2 + \gamma_1}{2} \right) + 8g^4 n + 2g^2 n \gamma_1 \left(\frac{\kappa_2 + \gamma_1}{2} \right) - 4g^4 (n+1)^2 \Bigg] x \quad \text{(B.2)}$$

This can be further simplified upon the assumption that $\frac{1}{T_2}$ is large, as shown in equation (2.31).

Unfortunately, the inverse Laplace transform of equation (2.32) is unwieldy and lends little insight to the nature of the system. In order to make this problem tractable, it is necessary to approximate the roots of the denominator of equation (2.32).

The solution to the equation

$$s^4 + \kappa s^3 + \frac{1}{4}\kappa^2 s^2 + \frac{1}{4}\kappa^2 \gamma_1 s + \kappa g^2 \gamma_1 (n+1) = 0 \quad \text{(B.3)}$$

lies in two distinct regimes of s. The first regime is $\frac{s}{\kappa} \ll 1$, and rearranging equation (B.3)

$$\frac{s^4}{\kappa^2} + \frac{s^3}{\kappa} + \frac{s(s+\gamma_1)}{4} + \frac{g^2 \gamma_1 (n+1)}{\kappa} = 0 \quad \text{(B.4)}$$

we see that in this regime, the largest relevant term (which will be of order κ^0) is

$$\frac{s(s+\gamma_1)}{4} = 0 \quad \text{(B.5)}$$

The solutions to equation (B.5) are $\tilde{s}_1 = 0$ and $\tilde{s}_2 = -\gamma_1$. However, these solutions are of insufficient accuracy to allow for a valid solution of equation

(2.32). In particular, $\tilde{s}_1 = 0$ will lead to undamped growth of $x(t)$, which is nonphysical.

Thus, it is necessary to find solutions to equation (B.3) of the form $s_1 = \tilde{s}_1 + \delta s_1$ and $s_2 = \tilde{s}_2 + \delta s_2$, where δs_1 and δs_2 will be of the next highest order, which is κ^{-1}. Substituting these expressions for s_1 and s_2 into equation (B.4) results in the following solutions, of order up to κ^{-1}.

$$s_1 = -\frac{g^2(n+1)}{\kappa} \tag{B.6}$$

$$s_2 = -\gamma_1 - \frac{4(\gamma_1^2 - g^2(n+1))}{\kappa} \tag{B.7}$$

We can understand these roots as a manifestation of Fermi's golden rule. Dephasing in the detector broadens its line as seen from the cavity, and also lowers its height to $1/\kappa$, hence this term appears in both rates. Rate 1 is then the rate of incoherent emission of energy from the detector back to the cavity, rate 2 contains tunnelling to lowest order and, again, emission back to the cavity as well as incoherent tunnelling as corrections.

The other two roots are to be found in the second regime, characterised by $\frac{s}{\kappa} \sim 1$. In this regime, the highest order terms are of order κ^2, and equation (B.4) becomes

$$\frac{s^4}{\kappa^2} + \frac{s^3}{\kappa} + \frac{s^2}{4} = 0 \tag{B.8}$$

The $s = 0$ roots of equation (B.8) lie outside of the domain of interest, so they can be ignored, which leaves

$$\frac{s^2}{\kappa^2} + \frac{s}{\kappa} + \frac{1}{4} = 0 \tag{B.9}$$

The solution to equation (B.9) is

$$s_3 = s_4 = -\frac{\kappa}{2} \tag{B.10}$$

Using the approximate roots of equations (B.6), (B.7), and (B.10), an approximate solution for $X(s)$ can be found, and this will have a simpler inverse Laplace transform.

$$X(s) \approx 2g^2(n+1)x_0 \left(\frac{s + \frac{\kappa - 3\gamma_1}{2}}{(s+\frac{\kappa}{2})^2 (s + \frac{g^2(n+1)}{\kappa})(s + \gamma_1 + \frac{4(\gamma_1^2 - g^2(n+1))}{\kappa})} \right) \tag{B.11}$$

As the inverse Laplace transform of equation (B.11) is simple to calculate, a solution for $x(t) = \mathcal{L}^{-1}[X(s)]$ can easily be obtained. Using this and equation (2.30), one can easily obtain the occupation probability of the cavity state $|n\rangle \langle n|_c$, given that a measurement has occurred.

$$\begin{aligned}
\langle n|_c \, \rho_{mm}(t) \, |n\rangle_c &= \gamma_1 \int \langle n|_c \, \hat{\rho}_{11}(t) \, |n\rangle_c \, dt = \gamma_1 \int x(t) dt \\
&= 4g^2\kappa^2\gamma_1(1+n)x_0 \Bigg(\frac{6e^{-\frac{\kappa t}{2}}(2+\kappa t)\gamma_1}{\kappa^2(\kappa^2 - 8g^2(1+n))(\kappa^2 + 8g^2(1+n) - 2\kappa\gamma_1 - 8\gamma_1^2)} + \frac{e^{\frac{-4g^2(1+n)t}{\kappa}} \kappa(\kappa(\kappa - 3\gamma_1) - 8g^2(1+n))}{4(1+n)(g\kappa^2 - 8g^3(1+n))^2(8g^2(1+n) - \gamma_1(\kappa+4\gamma_1))} \\
&+ \frac{e^{\frac{(4g^2(1+n) - \gamma_1(\kappa+4\gamma_1))t}{\kappa}} \kappa(\kappa^2 + 8g^2(1+n) - 5\kappa\gamma_1 - 8\gamma_1^2)}{(\kappa^2 + 8g^2(1+n) - 2\kappa\gamma_1 - 8\gamma_1^2)^2 (8g^2(1+n) - \gamma_1(\kappa+4\gamma_1))(4g^2(1+n) - \gamma_1(\kappa+4\gamma))} \\
&+ \frac{4e^{\frac{-\kappa t}{2}}(64g^4(1+n)^2 - 16g^2(1+n)\gamma_1(\kappa+4\gamma_1) - \kappa(\kappa^3 - 8\kappa^2\gamma_1 - 2\kappa\gamma_1^2 + 24\gamma_1^3))}{\kappa(64g^4(1+n)^2 - 16g^2(1+n)\gamma_1(\kappa+4\gamma_1) - \kappa^2(\kappa^2 - 2\kappa\gamma_1 - 8\gamma_1^2))^2} \Bigg)
\end{aligned} \tag{B.12}$$

Substituting the set of values of n, from $n = 0$ up to the highest photon number of the cavity, into equation (B.12) will result in a set of solutions describing the occupation probabilities of the states $\{\langle n|_c \, \rho_{\mathrm{mm}}(t) \, |n\rangle_c\}_{n=0}^{N}$. From this we obtain the probability of detection which is given by

$$P_{\mathrm{det}} = \sum_{n=0}^{N} \langle n|_c \, \rho_{\mathrm{mm}}(t) \, |n\rangle_c \, , \tag{B.13}$$

where N is the maximum number of photons in the cavity.

In addition to detection probability, in light of equation (2.26) it is possible to solve for any matrix element, $\langle i|_{\mathrm{c}}\, \rho_{\mathrm{mm}}(t)\, |j\rangle_{\mathrm{c}}$, of the reduced cavity state via the procedure used above to solve for the diagonal elements. Using this it is possible to construct the full density matrix of the reduced cavity state after a measurement has occurred.

B.2 Incoherent Tunnelling Model

To obtain equation (2.36), we rewrite the equations of (2.35) in matrix form

$$\partial_t \begin{pmatrix} P_0 \\ P_1 \\ P_m \end{pmatrix} = \begin{pmatrix} -\gamma_2 n & \gamma_2 n & 0 \\ \gamma_2 n & -(\gamma_1 + \gamma_2 n) & 0 \\ 0 & \gamma_1 & 0 \end{pmatrix} \begin{pmatrix} P_0 \\ P_1 \\ P_m \end{pmatrix} \tag{B.14}$$

where the index indicating the photon number in the cavity has been suppressed. The Laplace transform of this system of equations is

$$\begin{pmatrix} s\mathcal{P}_0 - 1 \\ s\mathcal{P}_1 \\ s\mathcal{P}_m \end{pmatrix} = \begin{pmatrix} -\gamma_2 n & \gamma_2 n & 0 \\ \gamma_2 n & -(\gamma_1 + \gamma_2 n) & 0 \\ 0 & \gamma_1 & 0 \end{pmatrix} \begin{pmatrix} \mathcal{P}_0 \\ \mathcal{P}_1 \\ \mathcal{P}_m \end{pmatrix} \tag{B.15}$$

where we have used the fact that $P_i(0) = \delta_{i0}$, and defined $\mathcal{P}_i(s) = \mathcal{L}[P_i(t)]$.

Solving the system of equations (B.15) for $\mathcal{P}_m(s)$ gives

$$\mathcal{P}_m(s) = \frac{n\gamma_1\gamma_2}{s\left(s^2 + s\left(2n\gamma_2 + \gamma_1\right) + n\gamma_1\gamma_2\right)}. \tag{B.16}$$

Using partial fractions and finding the residues of $\mathcal{P}_m$ at the poles allows us to rewrite equation (B.16) as follows:

$$\mathcal{P}_m(s) = \frac{1}{s} + \frac{\gamma_1\gamma_2 n}{s_+ - s_-}\left(\frac{1}{s_+(s - s_+)} - \frac{1}{s_-(s - s_-)}\right), \tag{B.17}$$

where $s_\pm$ are as defined in equation (2.37). The inverse Laplace transform of equation (B.17) can easily be calculated to obtain equation (2.36).

References

[1] Michael A. Nielsen and Isaac L. Chuang. *Quantum Computation and Quantum Information*. Cambridge University Press, 1 edition, 2000.

[2] Sergio M. Dutra. *Cavity Quantum Electrodynamics: The Strage Theory of Light in a Box*. Wiley Series in Lasers and Applications. Wiley, 2005.

[3] S. Haroche and J.-M. Raimond. *Exploring the Quantum: Atoms, Cavities, and Photons*. Oxford University Press, Oxford, 2006.

[4] Heinz-Peter Breuer and Francesco Petruccione. *The Theory of Open Quantum Systems*. Oxford University Press, 2006.

[5] Joseph Emerson. Amath 876: Open quantum systems lecture notes. Electronic, September 2009.

[6] Various. *Springer Handbook of Atomic, Molecular and Optical Physics*. Springer, 2006.

[7] S. Haroche and D. Kleppner. Cavity quantum electrodynamics. *Physics Today*, page 24, 1989.

[8] G. Rempe. Quantum mechanics with single atoms and photons. *Phys. World*, 13:37, 2000.

[9] H.J. Kimble. The quantum internet. *Nature*, 453:1023, 2008.

[10] D.I. Schuster, A.A. Houck, J.A. Schreiber, A. Wallraff, J.M. Gambetta, A. Blais, L. Frunzio, J. Majer, B.R. Johnson, M.H. Devoret, S.M. Girvin, and R.J. Schoelkopf. Resolving photon number states in a superconducting circuit. *Nature*, 445:515, 2007.

[11] A.A. Houck, D.I. Schuster, J.M. Gambetta, J.A. Schreier, B.R. Johnson, J.M. Chow, J. Majer, L. Frunzio, M.H. Devoret, S.M. Girvin, and R.J. Schoelkopf. Generating single microwave photons in a circuit. *Nature*, 449:328, 2007. cond-mat/0702648.

[12] P.J. Leek, J.M. Fink, A. Blais, R. Bianchetti, M. Goeppl, J.M. Gambetta, D.I. Schuster, L. Frunzio, R.J. Schoelkopf, and A. Wallraff. Observation of berry's phase in a solid state qubit. *Science*, 318:1889, 2007.

[13] O. Astafiev, K. Inomata, A.O. Niskanen, T. Yamamoto, Yu. A. Pashkin, Y. Nakamura, and J.S. Tsai. Single artificial-atom lasing. *Nature*, 449:558, 2007.

[14] A. Fragner, M. Goeppl, J.M. Fink, M. Baur, R. Bianchetti, P.J. Leek, A. Blais, and A. Wallraff. Resolving vacuum fluctuations in an electrical circuit by measuring the lamb shif. *Science*, 322:1357, 2008.

[15] M. Grajcar, S.H.W. van der Ploeg, A. Izmalkov, E. Il'ichev, H.-G. Meyer, A. Fedorov, A. Shnirman, and G. Schön. Sisyphus cooling and amplification by a superconducting qubit. *Nat. Phys.*, 4:612, 2008.

[16] M. Baur, S. Filipp, R. Bianchetti, J.M. Fink, M. Goeppl, L. Steffen, P.J. Leek, A. Blais, and A. Wallraff. Measurement of autler-townes and mollow transitions in a strongly driven superconducting qubit. *Phys. Rev. Lett.*, 102:243602, 2009.

[17] C. Lang, D. Bozyigit, C. Eichler, L. Steffen, J.M. Fink, A.A. Abdumalikov jr, M. Baur, S. Filipp, M.P. da Silva, A. Blais, and A. Wallraff.

Observation of resonant photon blockade at microwave frequencies using correlation function measurements. *Phys. Rev. Lett.*, 106:243601, 2011.

[18] Yu. Makhlin, G. Schön, and A. Shnirman. Quantum-state engineering with Josephson-junction devices. *Rev. Mod. Phys.*, 73:357, 2001.

[19] G. Wendin and V.S. Shumeiko. *Handbook of Theoretical and Computational Nanotechnology*, chapter Superconducting Quantum Circuits, Qubits and Computing. American Scientific Publishers, 2006.

[20] M.R. Geller, E.J. Pritchett, A.T. Sornborger, and F.K. Wilhelm. Quantum computing with superconductors i: Architectures. In M.E. Flatte and I. Tifrea, editors, *Manipulating quantum coherence in Solid State Systems*, Science Series II. Mathematics, Physics, and Chemistry, page 171, Dordrecht, 2007. Nato, Springer. quant-ph/0603224.

[21] J. Clarke and F.K. Wilhelm. Superconducting qubits. *Nature*, 453:1031, 2008.

[22] J.Q. You and F. Nori. Superconducting circuits and quantum information. *Phys. Today*, 58:42, 2005.

[23] A. Blais, R-S. Huang, A. Wallraff, S.M. Girvin, and R.J. Schoelkopf. Cavity quantum electrodynamics for superconducting electrical circuits: An architecture for quantum computing. *Phys. Rev. A*, 69:062320, 2004.

[24] A. Wallraff, D.I. Schuster, A. Blais, L. Frunzio, R.S. Huang, J. Majer, S. Kumar, S.M. Girvin, and R.J. Schoelkopf. Strong coupling of a single photon to a superconducting qubit using circuit quantum electrodynamics. *Nature*, 431:162, 2004.

[25] R.J. Schoelkopf and S.M. Girvin. Wiring up quantum systems. *Nature*, 451:664, 2008.

[26] F. Helmer, M. Mariantoni, A.G. Fowler, J. von Delft, E. Solano, and F. Marquardt. Two-dimensional cavity grid for scalable quantum computation with superconducting circuits. *EPL*, 76:50007, 2009.

[27] D.P. DiVincenzo. Fault-tolerant architectures for superconducting qubits. *Phys. Scr.*, T137:014020, 2009.

[28] M. Devoret, S. Girvin, and R.J. Schoelkopf. Circuit-qed: How strong can the coupling between a josephson junction atom and a transmission line resonator be? *Ann. Phys. (Leipzig)*, 16:767, 2007.

[29] M. Hofheinz, H. Wang, M. Ansmann, R.C. Bialczak, E. Lucero, M. Neeley, A.D. O'Connell, D. Sank, J. Wenner, J.M. Martinis, and A.N. Cleland. Synthesizing arbitrart quantum states in a superconducting resonator. *Nature*, 459:546, 2009.

[30] J. Bourassa, J.M. Gambetta, A.A. Abdumalikov, O. Astafiev, Y. Nakamura, and A. Blais. Ultrastrong coupling regiome of cavity qed with phase-biased flux qubits. *Phys. Rev. A*, 80:032109, 2009.

[31] J. Casanova, G. Romero, I. Lizuain, J.J. Garcia-Ripoll, and E. Solano. Deep strong coupling regime of the jaynes cummings model. *Phys. Rev. Lett.*, 105:263603, 2010.

[32] P. Forn-Diaz, J. Lisenfeld, D. Marcos, J.J. Garcia-Ripoll, E. Solano, C.J.P.M. Harmans, and J.E. Mooij. Observation of the bloch-siegert shift in a qubit-oscillator system in the ultrastrong coupling regime. *Phys. Rev. Lett.*, 105:237001, 2010.

[33] T. Niemczyk, F. Deppe, H. Huebl, E.P. Menzel, F. Hocke, M.J. Schwartz, J.J. Garcia-Ripoll, D. Zueco, T. Hummer, E. Solano, A. Marx, and R. Gross. Circuit quantum electrodynamics in the ultrastrong-coupling regime. *Nat. Phys.*, 6:772, 2010.

[34] C.M. Wilson, G. Johansson, A. Pourkabirian, M. Simoen, J.R. Johansson, T. Duty, F. Nori, and P. Delsing. Observation of the dynamical casimir effect in a superconducting circuit. *Nature*, 479:376, 2011.

[35] F. K. Wilhelm. Asymptotic von neumann measurement strategy for solid-state qubits. *Phys. Rev. B*, 68:060503, 2003.

[36] B.L. Osberg. Quantum microwave photo detection using superconducting josephson circuits. Master's thesis, University of Waterloo, 2009.

[37] G. Romero, J. J. García-Ripoll, and E. Solano. Microwave photon detector in circuit qed. *Phys. Rev. Lett.*, 102:173602, Apr 2009.

[38] Guillermo Romero, Juan José García-Ripoll, and Enrique Solano. Photodetection of propagating quantum microwaves in circuit qed. *Physica Scripta*, 2009(T137):014004, 2009.

[39] A.O. Caldeira and A.J. Leggett. Influence of dissipation on quantum tunneling in macroscopic systems. *Phys. Rev. Lett.*, 46:211, 1981.

[40] A.O. Caldeira and A.J. Leggett. Quantum tunneling in a dissipative system. *Ann. Phys. (NY)*, 149:374, 1983.

[41] K.S. Chow and V. Ambegaokar. Transition from quantum to classical dissipation in the problem of escape from a metastable well: Application to josephson junctions. *Physical Review B*, 38-16:11168–11176, 1988.

[42] K.S. Chow, D. A. Browne, and V. Ambegaokar. Quantum kinetics of a superconducting tunnel junction: Theory and comparison with experiment. *Physical Review B*, 17-4:1624–1646, 1988.

[43] J.M. Martinis, M.H. Devoret, and J. Clarke. Energy-level quantization in the zero-voltage state of a current-biased Josephson junction. *Phys. Rev. Lett.*, 55(15):1543–1546, 1985.

[44] J.M. Martinis, M.H. Devoret, and J. Clarke. Experimental tests for the quantum behavior of a macroscopic degree of freedom: The phase difference across a Josephson junction. *Phys. Rev. B*, 35(10):4682–4698, 1987.

[45] Y.-F. Chen, D. Hover, S. Sendelbach, L. Maurer, S. T. Merkel, E. J. Pritchett, F. K. Wilhelm, and R. McDermott. Microwave photon counter based on josephson junctions. *Phys. Rev. Lett.*, 107:217401, Nov 2011.

[46] J.M. Martinis, S. Nam, J. Aumentado, and C. Urbina. Rabi oscillations in a large Josephson-junction qubit. *Phys. Rev. Lett.*, 89(11):117901, 2002.

[47] J.M. Martinis. Superconducting phase qubits. *Quantum Information Processing*, 8:81, 2009.

[48] M. Mück, J.B. Kycia, and J. Clarke. Superconducting quantum interference device as a near-quantum-limited amplifier at 0.5 ghz. *Appl. Phys. Lett.*, 78:967, 2001.

[49] M. Muck, C. Welzel, and J. Clarke. Superconducting quantum interference device amplifiers at gigahertz frequencies. *Appl. Phys. Lett.*, 82(19):3266–3268, 2003.

[50] D. Hover, Y.-F. Chen, G.J. Ribelli, S. Zhu, and R. McDermott. Superconducting low-inductance undulatory galvanometer microwave amplifier. arXiv:1109.5209, accepted at Appl. Phys. Lett.

[51] G.J. Ribelli, D. Hover, Y.-F. Chen, S. Zhu, and R. McDermott. Superconducting low-inductance undulatory galvanometer microwave amplifier: Theory. *J. Appl. Phys.*, 110:103901, 2011.

[52] M.P. deFeo, P. Bhupathi, K. Yu, T.W. Heitmann, C. Song, R. McDermott, and B.L.T. Plourde. Microstrip superconducting quantum

interference device amplifiers with submicron josephson junctions: Enhanced gain at gigahertz frequencies. *Appl. Phys. Lett.*, 97:092507, 2010.

[53] N. Bergeal, F. Schackert, M. Metcalfe, R. Vijay, V.E. Manucharyan, L. Frunzio, D.E. Prober, R.J. Schoelkopf, S.M. GIrvin, and M.H. Devoret. Phase preserving amplification near the quantum limit with a josephson ring modulator. *Nature*, 465:64, 2010. arXiv:0912.3407.

[54] M.A. Castellanos-Beltran, K.D. Irwin, G.C. Hilton, L.R. Vale, and K.W. Lehnert. Amplification and squeezing of quantum noise with a tunable josephson metamaterial. *Nat. Phys.*, 4:929, 2008.

[55] M. Hatridge, R. VIjay, D.H. Slichter, J. Clarke, and I. Siddiqi. Dispersive magnetometry with a quantum limited squid parametric amplifier. *Phys. Rev. B*, 83:134501, 2011.

[56] A.A. Clerk, M.H. Devoret, S.M. Girvin, F. Marquardt, and R.J. Schoelkopf. Introduction to quantum noise, measurement, and amplification. *Rev. Mod. Phys.*, 82:1155, 2010.

[57] M. Mariantoni, M.J. Storcz, F.K. Wilhelm, W.D. Oliver, A. Emmert, A. Marx, R. Gross, H. Christ, and E. Solano. On-chip microwave fock states and quantum homodyne measurements. cond-mat/0509737.

[58] M.P. da Silva, D. Bozyigit, A. Wallraff, and A. Blais. Schemes for the observation of photon correlation functions in circuit qed with linear detectors. *Phys. Rev. A*, 82(043804), 2010.

[59] E.P. Menzel, F. Deppe, M. Mariantoni, M.A.A. Caballero, A. Baust, T. Niemczyk, E. Hoffmann, A. Marx, E. Solano, and R. Gross. Dual-path state reconstruction scheme for propagating quantum microwaves and detector noise tomography. *Phys. Rev. Lett.*, 105:100401, 2010.

[60] D. Bozyigit, C. Lang, L. Steffen, J.M. Fink, M. Baur, R. Bianchetti, P.J. Leek, S. Filipp, M.P. da Silva, A. Blais, and A. Wallraff. Measurements of the correlation function of a microwave frequency single photon source. *Nat. Phys.*, 7:154, 2011. arXiv:1002.3738.

[61] F. Mallet, M.A. Castellanos-Beltran, H.S. Ku, S. Glancy, E. Knill, K.D. Irwin, G.C. Hilton, L.R. Vale, and K.W. Lehnert. Quantum state tomography of an itinerant squeeze microwave field. *Phys. Rev. Lett.*, 106:220502, 201.

[62] M.G.A. Paris and J. Rehacek. *Quantum State Estimation.* Springer, Berlin, 2004.

[63] A.I. Lvovsky and M.G. Raymer. Continuous-variable optical quantum-state tomography. *Rev. Mod. Phys.*, 81:299, 2009.

[64] M. Sarovar and K.B. Whaley. Adaptive homodyne phase discrimination and qubit measurement. *Phys. Rev. A*, 76:052316, 2007.

[65] R.W. Simmonds, K.M. Lang, D.A. Hite, D.P. Pappas, and J.M. Martinis. Decoherence in josephson qubits from junction resonances. *Phys. Rev. Lett.*, 93:077003, 2004.

[66] M. Goeppl, A. Fragner, M. Baur, R. Bianchetti, S. Filipp, J.M. Fink, P.J. Leek, G. Puebla, L. Steffen, and A. Wallraff. Coplanar waveguide resonators for circuit quantum electrodynamics. *J. Appl. Phys.*, 104:113904, 2008.

[67] A. Megrant, C. Neill, R. Barends, B. Chiaro, Y. Chen, L. Feigl, J. Kelly, E. Lucero, M. Mariantoni, P.J.J. O'Malley, D. Sank, A. Vaisencher, J. Wenner, T.C. White, Y. Yin, J. Zhao, C.J. Palmstrøm, and J.M. Martinis. Planar superconducting resonators with internal quality factors above one million. arXiv:1201.3384.

[68] M. Mohseni, A. T. Rezakhani, and D. A. Lidar. Quantum-process tomography: Resource analysis of different strategies. *Phys. Rev. A*, 77:032322, Mar 2008.

[69] M. Hofheinz, E.M. Weig, M. Ansmann, R.C. Bialczak, E. Lucero, M. Neeley, A.D. O'Connell, H. Wang, and J.M. Martinis. Generation of fock states in a superconducting quantum circuit. *Nature*, 454:310, 2008.

[70] H.J. Carmichael. *Statistical Methods in Quantum Optics*. Springer, Berlin, 1999.

[71] L. Susskind and J. Glogower. Quantum mechanical phase and time operator. *Physics*, 49:1, 1964.

[72] D.T. Pegg and S.T. Barnett. Phase properties of the quantized single-mode electromagnetic field. *Phys. Rev. A*, 39:1665, 1989.

[73] I. Serban, E Solano, and F.K. Wilhelm. Crossover from weak- to strong-coupling regime in dispersive circuit qed. *Europhys. Lett.*, 80:40011, 2007. cond-mat/0606734.

[74] I. Serban, E. Solano, and F.K. Wilhelm. Phase-space theory for dispersive detectors of superconducting qubits. *Phys. Rev. B*, 76:104510, 2007.

[75] T. L. Robertson, B. L. T. Plourde, T. Hime, S. Linzen, P. A. Reichardt, F. K. Wilhelm, and John Clarke. Superconducting quantum interference device with frequency-dependent damping: Readout of flux qubits. *Phys. Rev. B*, 72:024513, Jul 2005.

[76] Alexei Ourjoumtsev, Rosa Tualle-Brouri, Julien Laurat, and Philippe Grangier. Generating optical schrdinger kittens for quantum information processing. *Science*, 312(5770):83–86, 2006.

[77] M. Dakna, T. Anhut, T. Opatrný, L. Knöll, and D.-G. Welsch. Generating schrödinger-cat-like states by means of conditional measurements on a beam splitter. *Phys. Rev. A*, 55:3184–3194, Apr 1997.

[78] C. Eichler, D. Bozyigit, C. Lang, M. Baur, L. Steffen, J. M. Fink, S. Filipp, and A. Wallraff. Observation of two-mode squeezing in the microwave frequency domain. *Phys. Rev. Lett.*, 107:113601, Sep 2011.

[79] M.K. Akhlaghi, A.H. Majedi, and J.S. Lundeen. Nonlinearity in single photon detection: modeling and quantum tomography. *Optics Express*, 19(22):21305–21312, 2011.

[80] Robert H. Hadfield. Single-photon detectors for optical quantum information applications. *Nat Photon*, 3(12):696–705, 12 2009.

[81] Luke C.G. Govia, Emily J. Pritchett, Seth T. Merkel, Deanna Pineau, and Frank K. Wilhelm. Theory of josephson photomultipliers: Optimal working conditions and back action. arXiv:1206.0360, 2012.

[82] Hans J. Weber George B. Arfken and Frank E. Harris. *Mathematical Methods for Physicists: A Comprehensive Guide*. Academic Press, 7 edition, January 2012.

[83] János K. Asbóth, John Calsamiglia, and Helmut Ritsch. Computable measure of nonclassicality for light. *Phys. Rev. Lett.*, 94:173602, May 2005.

[84] G. Vidal and R. F. Werner. Computable measure of entanglement. *Phys. Rev. A*, 65:032314, Feb 2002.

[85] H. Wiseman and G. Milburn. *Quantum Measurement and Control*. Cambridge University Press, 2010.

[86] Karl Blum. *Density Matrix Theory and Applications*. Springer, 3 edition, 2012.

[87] Roger A. Horn and Charles R. Johnson. *Matrix Analysis*. Cambridge University Press, June 1990.

[88] G. Dirr, U. Helmke, I. Kurniawan, and T. Schulte-Herbrüggen. Lie-semigroup structures for reachability and control of open quantum systems: kossakowski-lindblad generators form lie wedge to markovian channels. *Reports on Mathematical Physics*, 64(1-2):93 – 121, 2009.

[89] C. O'Meara, G. Dirr, and T. Schulte-Herbrüggen. Illustrating the geometry of coherently controlled unital open quantum systems. *IEEE Transactions on Automatic Control*, 57(8), 2012.